Monthly Notices
of the
ROYAL ASTRONOMICAL SOCIETY

MNRAS **526,** 1343–1366 (2023) https://doi.org/10.1093/mnras/stad2545
Advance Access publication 2023 August 25

QUIJOTE scientific results – X. Spatial variations of Anomalous Microwave Emission along the Galactic plane

M. Fernández-Torreiro,[1,2★] J. A. Rubiño-Martín,[1,2★] C. H. López-Caraballo,[1,2] R. T. Génova-Santos,[1,2] M. W. Peel,[1,2] F. Guidi,[1,2,3] S. E. Harper,[4] E. Artal,[5] M. Ashdown,[6,7] R. B. Barreiro,[8] F. J. Casas,[8] E. de la Hoz,[8,9] D. Herranz,[8] R. Hoyland,[1,2] A. Lasenby,[6,7] E. Martínez-Gonzalez,[8] L. Piccirillo,[4] F. Poidevin,[1,2] R. Rebolo,[1,2,10] B. Ruiz-Granados,[1,2,11] D. Tramonte,[1,2,12] F. Vansyngel,[1,2] P. Vielva[8] and R. A. Watson[4]

[1] *Instituto de Astrofísica de Canarias, E-38200 La Laguna, Tenerife, Spain*
[2] *Departamento de Astrofísica, Universidad de La Laguna, E-38206 La Laguna, Tenerife, Spain*
[3] *Institut d'Astrophysique de Paris, UMR 7095, CNRS & Sorbonne Université, 98 bis boulevard Arago, F-75014 Paris, France*
[4] *Jodrell Bank Centre for Astrophysics, Alan Turing Building, Department of Physics & Astronomy, School of Natural Sciences, The University of Manchester, Oxford Road, Manchester M13 9PL, UK*
[5] *Universidad de Cantabria, Departamento de Ingeniería de Comunicaciones, Edificio Ingenieria de Telecomunicación, Plaza de la Ciencia 1, E-39005 Santander, Spain*
[6] *Astrophysics Group, Cavendish Laboratory, University of Cambridge, J J Thomson Avenue, Cambridge CB3 0HE, UK*
[7] *Kavli Institute for Cosmology, University of Cambridge, Madingley Road, Cambridge CB3 0HA, UK*
[8] *Instituto de Física de Cantabria (IFCA), CSIC-Univ. de Cantabria, Avda. los Castros, s/n, E-39005 Santander, Spain*
[9] *Departamento de Física Moderna, Universidad de Cantabria, Avda. de los Castros s/n, E-39005 Santander, Spain*
[10] *Consejo Superior de Investigaciones Científicas, E-28006 Madrid, Spain*
[11] *Departamento de Física. Facultad de Ciencias. Universidad de Córdoba. Campus de Rabanales, Edif. C2. Planta Baja. E-14071 Córdoba, Spain*
[12] *Department of Physics, Xi'an Jiaotong-Liverpool University, 111 Ren'ai Road, Suzhou Dushu Lake Science and Education Innovation District, Suzhou Industrial Park, Suzhou 215123, P.R. China*

Accepted 2023 August 4. Received 2023 June 14; in original form 2023 February 7

ABSTRACT

Anomalous microwave emission (AME) is an important emission component between 10 and 60 GHz that is not yet fully understood. It seems to be ubiquitous in our Galaxy and is observed at a broad range of angular scales. Here we use the new QUIJOTE-MFI wide survey data at 11, 13, 17, and 19 GHz to constrain the AME in the Galactic plane ($|b| < 10^\circ$) on degree scales. We built the spectral energy distribution between 0.408 and 3000 GHz for each of the 5309 0.9° pixels in the Galactic plane, and fitted a parametric model by considering five emission components: synchrotron, free–free, AME, thermal dust and CMB anisotropies. We show that not including QUIJOTE-MFI data points leads to the underestimation (up to 50 per cent) of the AME signal in favour of free–free emission. The parameters describing these components are then intercompared, looking for relations that help to understand AME physical processes. We find median values for the AME width, $W_{\rm AME}$, and for its peak frequency, $\nu_{\rm AME}$, respectively of $0.560^{+0.059}_{-0.050}$ and $20.7^{+2.0}_{-1.9}$ GHz, slightly in tension with current theoretical models. We find spatial variations throughout the Galactic plane for $\nu_{\rm AME}$, but only with reduced statistical significance. We report correlations of AME parameters with certain ISM properties, such as that between the AME emissivity (which shows variations with the Galactic longitude) and the interstellar radiation field, and that between the AME peak frequency and dust temperature. Finally, we discuss the implications of our results on the possible molecules responsible for AME.

Key words: radiation mechanisms:general – ISM: general – Galaxy: general – diffuse radiation – radio continuum: ISM.

1 INTRODUCTION

The first detections of Galactic anomalous microwave emission (AME) were carried out less than 30 years ago (Kogut et al. 1996; Leitch et al. 1997): the Differential Microwave Radiometers (DMR, Smoot et al. 1990) onboard of the Cosmic Bakground Explorer (COBE; Boggess et al. 1992), recorded an unexpected excess emission at 31 GHz. This excess was first thought to be due to free–free or synchrotron components. However, this emission did not correlate with Hα emission, which is expected for free–free,[1] and was not polarized, as synchrotron is. This supported a scenario with a fresh new emission component that was important important through the 10–60 GHz frequency range (de Oliveira-Costa et al. 1999; Watson et al. 2005; Hildebrandt et al. 2007). This

---

★ E-mail: mateo.fernandez@iac.es (MFT); jalberto@iac.es (JARM)

[1] In absence of extreme conditions, such as in compact H II regions.

new component was named 'anomalous microwave emission', or AME. Further Galactic (Dickinson et al. 2009; Todorović et al. 2010; Génova-Santos et al. 2011; Planck Collaboration 2014b; Battistelli et al. 2019; Rennie et al. 2022) and extragalactic (Murphy et al. 2010; Scaife et al. 2010; Hensley, Murphy & Staguhn 2015; Murphy et al. 2018; Linden et al. 2020) AME sources have since been identified, with studies also providing upper levels when a detection was not achievable (Peel et al. 2011; Planck Collaboration 2015b; Tibbs et al. 2018; Bianchi et al. 2022).

The emission mechanism for this new component is not yet clear, but the most popular hypothesis states that electric dipole emission from spinning dust grains is responsible for this excess signal (Erickson 1957; Draine & Lazarian 1998a,b). This would explain the correlation between AME and mid-infrared dust emission (de Oliveira-Costa et al. 1997; Davies et al. 2006). Nevertheless, recent results have proposed that polycyclic aromatic hydrocarbons (PAHs) may not be as important as first thought, with generic very small grain (VSG) emission being more prominent (Hensley, Draine & Meisner 2016; Hensley & Draine 2017). This would be supported by a higher correlation between AME and the dust emission at 24–60 μm, instead of that measured at 8–12 μm (dominated by PAHs; Li & Draine 2001; Draine & Li 2007). Large amorphous carbon or silicates ($a_0 \in (1, 100)$ nm Compiègne et al. 2011), generically referred to as dust big grains (BGs) have been proposed also as AME carriers (Chuss et al. 2022): in that case, AME would correlate more strongly with 100–350 μm emission bands. Finally, the other main hypothesis for AME states that it could also be due to dust grains inside a magnetic field, which aligns the grains that emit radiation when their minimum energy state is reached (Draine & Lazarian 1999). This implies that, unlike in the spinning dust theory, the emission would be thermal.

However, both hypotheses have their disadvantages. In the magnetic field scenario, these are the current upper limits on polarization for AME emission. According to recent data (López-Caraballo et al. 2011; Rubiño-Martín et al. 2012; Génova-Santos et al. 2015; Poidevin et al. 2019; Tramonte et al. 2023), the AME polarized emission fraction is $\lesssim$5 per cent, with the strongest constrains being $\lesssim$0.5 per cent (Génova-Santos et al. 2017). A higher value is predicted in most magnetic models (Draine & Lazarian 1999; Draine & Hensley 2013; Hoang & Lazarian 2016). The problem with the spinning dust hypothesis, on the other hand, is the difficulty involved in the study of grain theory, where several parameters have a direct influence on the spectral shape emission (Ali-Haïmoud, Hirata & Dickinson 2009; Ysard, Juvela & Verstraete 2011; Ali-Haïmoud 2013). For a more detailed and comprenhesive review on AME, see Dickinson et al. (2018).

In this paper, using the new data between 10 and 20 GHz from the Multi-Frequency Instrument (hereafter, MFI) mounted on the Q-U-I JOint Tenerife Experiment (from now on, QUIJOTE), we aim to analyse how the parameters describing the AME vary along the Galactic plane. Spatial variations of AME properties have been hinted at in the past for sub-degree scales (Dickinson et al. 2010; Tibbs et al. 2013; Battistelli et al. 2015; Arce-Tord et al. 2020; Casassus et al. 2021), although mainly using interferometers. However, variations at degree scales have been measured only recently (Cepeda-Arroita et al. 2021), with the addition of medium-size telescopes focused on frequencies just below those studied by the WMAP and *Planck* satellites. The addition of ancillary data will further allow us to build a map of diffuse Galactic emission while assuming more relaxed priors than previous studies (Planck Collaboration 2014a, PL16; Andersen et al. 2023). These data also allow us better to understand the AME from the phenomenological point of view, along with the other foregrounds. Precise knowledge concerning these foregrounds (especially synchrotron, which greatly benefits from the addition of more frequency points below 20 GHz and is also present in polarization) will be essential for future missions focusing on CMB B-mode studies, such as the LiteBIRD satellite (Hazumi et al. 2020).

This paper is organized as follows. Section 2 gives an overview of the data set used to build the intensity spectral energy distributions (SEDs). The components describing these SEDs are then explained in Section 3, together with the Monte Carlo Markov Chain (MCMC) analysis applied. Section 4 presents the main results of the paper, and Section 5 compares these results with previous studies. Finally, in Section 6, we summarize the work done.

2 INPUT DATA

This paper is part of the QUIJOTE-MFI Wide Survey (Rubiño-Martín et al. 2023) Release and exploits the survey's new 10–20 GHz data. We built intensity SEDs in the radio domain for the Galactic plane $b \in (-10^\circ, +10^\circ)$ region. The parts of the Galactic plane that are not visible in all QUIJOTE-MFI bands (i.e. the equatorial band $\delta \in (-10^\circ, 0^\circ)$[2] and the southern sky $\delta < -32^\circ$) were not studied. Together with the QUIJOTE-MFI data, another 19 maps, listed in Table 1, were used and are described in the following subsections. Fig. 1 shows four examples of these maps.

All maps were smoothed to 1° beam resolution at their native pixelization, and then downgraded to HEALPIX[3] (Górski et al. 2005) $N_{\rm side} = 64$ pixelization, where each pixel has an angular size of $\simeq$0.9°. We can assume then that each pixel on the maps is almost uncorrelated with its neighbours, as the resolution of the maps matches the pixel size. Therefore, the area of study corresponds to 5309 regions, one per pixel ($f_{\rm sky} \approx 11$ per cent), after discarding the southern sky and the equatorial band.

2.1 QUIJOTE-MFI data

The QUIJOTE CMB experiment (Rubiño-Martín et al. 2010) operates from Teide Observatory (OT) of the Instituto de Astrofísica de Canarias (IAC), located at latitude 28°18′04″ North and longitude 16°30′38″ West. This latitude allows the telescopes to reach declinations as low as −32°, hence permitting partial coverage of the South Hemisphere sky. A collaboration between the IAC, the Instituto de Física de Cantabria (IFCA), Cambridge University, Manchester University, the Departamento de Ingenieria de Comunicaciones (DICOM) from the Universidad de Cantabria and IDOM, QUIJOTE consists of two identical telescopes on Cross-Dragone optics and 2.25 m primary apertures. An altazimuth mount was chosen to allow the telescope to spin fast at a constant elevation while observing (the so-called 'nominal' mode) with a scanning speed of $12^\circ\,{\rm s}^{-1}$.

The MFI was the first science instrumentation mounted on the QUIJOTE experiment (specifically, on its first telescope). It observed simultaneously in four distinct bands with 2 GHz bandwidths and central frequencies 11, 13, 17, and 19 GHz. The MFI consisted of four horns or antennas, each observing at two frequencies: horns 1 and 3 observed at the lower frequencies (11 and 13 GHz), and horns 2 and 4 observed at 17 and 19 GHz. It came into operation in 2012, while the wide survey observations were run between 2013 and 2018. These observations were done in the 'nominal' configuration

---

[2] Due to Radio Frequency Interference (RFI) contamination from geostationary satellites, which emit close to 11–13 GHz (Rubiño-Martín et al. 2023).

[3] https://healpix.sourceforge.io/

Table 1. Surveys used in this study. Effelsberg and Parkes (SPASS) surveys have been used only for the Stockert/Villa-Elisa and HartRAO surveys recalibrations, respectively. Each pixel SED uses only the maps covering that pixel. Under the column ‘Calibration’, we quote the values used in this study to estimate the calibration uncertainty.

Telescope	Frequency (GHz)	Calibration (%)	FWHM (arcmin)	Sky coverage	Reference
Various	0.408	10	51	All-sky	Haslam et al. (1982), Remazeilles et al. (2015)
Dwingeloo	0.82	10	72	$\delta > -7^\circ$	Berkhuijsen (1972)
Effelsberg	1.408	10	9.4	$l \in [240, 357]^\circ$ $b \in [-4, 4]^\circ$	Reich, Reich & Fuerst (1990), Reich, Reich & Furst (1997)
Stockert/Villa-Elisa	1.42	20	34.2	All-sky	Reich (1982), Reich & Reich (1986) Reich, Testori & Reich (2001), Paradis et al. (2012)
Parkes (SPASS)	2.303	5	8.9	$\delta < -1^\circ$	Carretti et al. (2019)
HartRAO	2.326	20	20	$\delta < 13^\circ$	Jonas, Baart & Nicolson (1998), Platania et al. (2003)
QUIJOTE-MFI	11.2	5	53.2	$\delta > -32^\circ$	Rubiño-Martín et al. (2023)
QUIJOTE-MFI	12.9	5	53.5	$\delta > -32^\circ$	Rubiño-Martín et al. (2023)
QUIJOTE-MFI	16.8	5	39.1	$\delta > -32^\circ$	Rubiño-Martín et al. (2023)
QUIJOTE-MFI	18.7	5	39.1	$\delta > -32^\circ$	Rubiño-Martín et al. (2023)
WMAP K 9yr	22.8	3	51.3	All-sky	Bennett et al. (2013)
Planck-LFI PR3	28.4	3	33.1	All-sky	Planck Collaboration (2018)
WMAP Ka 9yr	33	3	39.1	All-sky	Bennett et al. (2013)
WMAP Q 9yr	40.7	3	30.8	All-sky	Bennett et al. (2013)
Planck-LFI PR3	44.1	3	27.9	All-sky	Planck Collaboration (2018)
WMAP V 9yr	60.7	3	21.0	All-sky	Bennett et al. (2013)
Planck-LFI PR3	70.4	3	13.1	All-sky	Planck Collaboration (2018)
WMAP W 9yr	93.5	3	14.8	All-sky	Bennett et al. (2013)
Planck-HFI PR3	143	3	7.3	All-sky	Planck Collaboration (2018)
Planck-HFI PR3	353	3	4.9	All-sky	Planck Collaboration (2018)
Planck-HFI PR3	545	6.1	4.8	All-sky	Planck Collaboration (2018)
Planck-HFI PR3	857	6.4	4.6	All-sky	Planck Collaboration (2018)
COBE-DIRBE 240 ZSMA	1249	11.6	37.1	All-sky	Hauser et al. (1998)
COBE-DIRBE 140 ZSMA	2141	10.6	38.0	All-sky	Hauser et al. (1998)
COBE-DIRBE 100 ZSMA	2998	13.5	38.6	All-sky	Hauser et al. (1998)

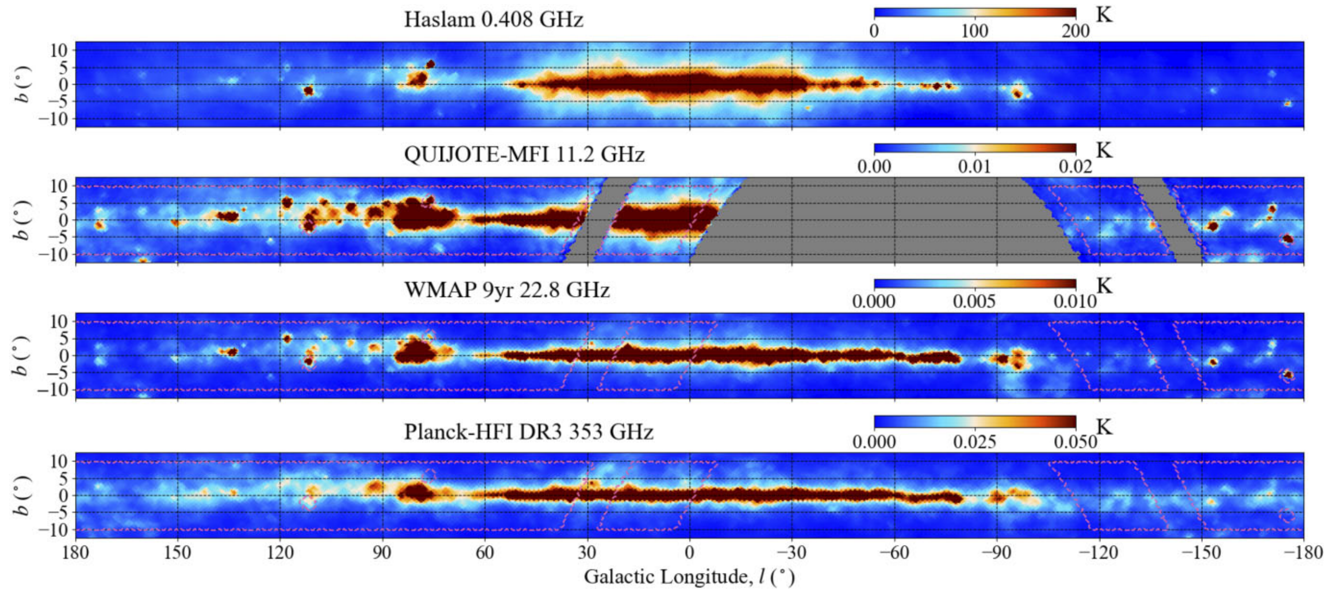

Figure 1. Examples of some of the frequency maps used in this study. From top to bottom: Haslam et al. (1982) at 0.408 GHz, QUIJOTE-MFI at 11.2 GHz, WMAP 9yr at 22.8 GHz, and *Planck-HFI* PR3 at 353 GHz. The first one and last two are good tracers for synchrotron, AME, and thermal dust emission, respectively. We also indicate the areas (shown with dashed-lines) studied in this study: those with $|b| < 10^\circ$ and $\delta \in (-32^\circ, -10^\circ)$ and $\delta > 0^\circ$. Some pixels with lower declinations are also observable by QUIJOTE-MFI (down to $\delta \approx -35^\circ$), but they are greatly affected by $1/f$ noise.

introduced before for a total of ∼10 000 h (Rubiño-Martín et al. 2023), during which all the sky accessible from the OT (more than 29 000 squared degrees) with scans of elevation higher or equal to 30° was observed.

The QUIJOTE-MFI first data release is presented in detail in Rubiño-Martín et al. (2023). It consists of a wide survey of the northern sky in four bands at 11.2, 12.9, 16.8, and 18.7 GHz, for both intensity and polarization. Sensitivities are better for polarization than for intensity: 35 − 40 µK deg^{-1} versus 60 − 200 µK deg^{-1}, respectively, owing to the lower 1/*f* noise in polarization. We use the combined maps between horns 2 and 4 (which are the publicly available ones) for 16.8 and 18.7 GHz, as the signal-to-noise ratio (SNR) is improved significantly from the non-combined case. Only the maps from horn 3 are used for the 11.2–12.9 GHz pair, as it has much better noise properties than horn 1. The calibration uncertainty is 5 per cent for all bands. Finally, we take into account that every pair of frequencies (11.2–12.9 or 16.8–18.7 GHz) observed with the same horn have correlations close to 80 per cent in intensity (Rubiño-Martín et al. 2023). This will be further explained when building the reconstructed SED for the pixels, in Section 3.3.1.

2.2 Ancillary low-frequency surveys

We used several low-frequency surveys in this work, which are summarized at the beginning of Table 1. In order to use them consistently with the full data set, some of them require a series of corrections, as explained in detail in this section.

The Berkhuijsen (1972) survey at 0.820 GHz accounts for an uncertainty equal to 0.3 K for systematic effects (unrelated to the determination of the zero level) between different areas of the sky. This transforms to 1.58 Jy at 0.820 GHz and HEALPIX $N_{\rm side} = 64$ pixel size. We have also increased its calibration uncertainty from 6 per cent to 10 per cent, owing to the clear presence of stripes in the map and its 72 arcmin angular resolution, which is slightly larger than the 1° used in the following analyses.

Moreover, Reich (1982), Reich & Reich (1986), and Reich et al. (2001) survey at 1.42 GHz and Jonas et al. (1998) survey at 2.326 GHz are calibrated to the full, 4π beam. As we are dealing with structures at the main-beam scale, multiplicative recalibration factors of 1.55 and 1.2 , respectively, should be applied to them. This is done in order to account for the flux density that is lost outside the main beam. Factors similar to these have been applied in past studies (Reich & Reich 1988; Planck Collaboration 2014b; Génova-Santos et al. 2017; Cepeda-Arroita et al. 2021). Irfan (2014) showed that the first value is consistent for a series of free–free-dominated emission regions. However, these factors are defined from observations of point sources. In the case of diffuse emission, this correction becomes milder, and these factors should be smaller. Because of this, we used a factor of 1.4 instead of 1.55 for the Reich (1982), Reich & Reich (1986), and Reich et al. (2001) survey. This was also done in the past, e.g. Planck Collaboration (2015b) when studying emission from M31. An even lower value (1.3) was used in that case, in fact. We estimated this value by comparing the map with that of Effelsberg suvey at 1.408 GHz (through TT-plot analyses) only for those pixels where diffuse emission is dominant over compact sources. For the Jonas et al. (1998) survey at 2.326 GHz, the recalibration factor remains equal to 1.2, as this was already consistent with TT-plot analyses comparing this map and the S-band Polarization All Sky Survey (SPASS, Carretti et al. 2019) one at 2.303 GHz. It is worth noting that before reducing the Reich (1982), Reich & Reich (1986), and Reich et al. (2001) survey factor to 1.4, we found systematically positive residuals at that frequency. This did not happen when dealing with the Jonas et al. (1998) survey.

Calibration uncertainties for both Reich (1982), Reich & Reich (1986), Reich et al. (2001), and Jonas et al. (1998) surveys were increased to ≃ 20 per cent. Even though the Jonas et al. (1998) recalibration factor was lower, this survey also had measured polarization (*Q*) with intensity, which further increased the uncertainty. Further discussion on this issue is presented in Appendix A. All the previously mentioned data are available in the Legacy Archive for Microwave Background Data Analysis (LAMBDA[4]).

2.3 WMAP, *Planck*, COBE-DIRBE

The Wilkinson Microwave Anisotropy Probe (WMAP; Bennett et al. 2013) and *Planck* (Planck Collaboration 2018) satellites produced full sky maps from 22.8 to 93.5 and from 28.4 to 857 GHz during 2001–2010 and 2009–2013, respectively. We used the WMAP 9-yr and *Planck* 2018 (PR3) data releases. WMAP data are publicly available on LAMBDA, and *Planck* data can be found through the *Planck* Legacy Archive (PLA[5]) hosted by the European Space Agency (ESA). The nominal calibration uncertainties for the WMAP and *Planck* bands calibrated against the CMB dipole (frequencies lower than 500 GHz) are extremely low (below 1 per cent, Planck Collaboration 2016a, hereafter PL16). However, we increased this value to 3 per cent to account for further inconsistencies, like beam uncertainties and colour correction uncertainties, which arise when dealing with foregrounds. This is, in fact, common through the literature (Planck Collaboration 2011, 2014b,2015a; Cepeda-Arroita et al. 2021). *Planck* bands calibrated using planetary data (545, 857 GHz) have higher calibration uncertainties, propagated from the theoretical models. We discarded *Planck* 100 and 217 GHz bands due to the contamination from CO emission.

The Diffuse Infrared Background Experiment (DIRBE, Hauser et al. 1998), mounted on the COBE satellite, observed the sky between 1250 GHz and 240 THz during 1989–1990: we used the average mission maps with subtracted zodiacal light. This latter experiment allowed us better to recover the high-frequency side of the thermal dust distribution. The data are available on LAMBDA.

2.4 Further map pre-processing

All the maps used in this study were filtered with the same filter used to remove the QUIJOTE-MFI residual RFI signal. This filter removes the zero mode in lines of constant declination, effectively reducing the large-scale power of the map ($\ell < 30$). This is done to ensure that all maps have the same effective window function. Further information on this correction is available in Rubiño-Martín et al. (2023; section 2.4.2 and appendix B).

3 METHODOLOGY

3.1 Foreground modelling

We considered five different emission components in our frequency range, between 0.4 and 3000 GHz: synchrotron, free–free, AME, thermal dust and CMB anisotropies. In this study, we adopted a parametric description for the flux density of these five components that is based on a set of 10 independent parameters, θ, as:

$$\begin{aligned} S_\nu^{\rm total}(\theta) = {} & S_\nu^{\rm syn}(I_{1\,{\rm GHz}}, \alpha_{\rm syn}) + S_\nu^{\rm ff}({\rm EM}) \\ & + S_\nu^{\rm AME}(I_{\rm AME}, \nu_{\rm AME}, W_{\rm AME}) \\ & + S_\nu^{\rm dust}(\tau_{353}, \beta_{\rm d}, T_{\rm d}) + \Delta S_\nu^{\rm CMB}(\Delta T_{\rm CMB}) \end{aligned} \quad (1)$$

which are described in the following subsections.

---

[4] https://lambda.gsfc.nasa.gov/

[5] http://pla.esac.esa.int/pla/#home

3.1.1 Synchrotron emission

Synchrotron emission is radiated by ultrarelativistic electrons accelerated by a magnetic field. Its spectral shape can be fitted as a power law (e.g. Rybicki & Lightman 1979; Condon & Ransom 2016):

$$S_\nu^{\rm syn}(I_{1\,{\rm GHz}}, \alpha_{\rm syn}) = I_{1\,{\rm GHz}} \left(\frac{\nu}{1\ {\rm GHz}}\right)^{\alpha_{\rm syn}} \Omega, \tag{2}$$

where $I_{1\,{\rm GHz}}$ is the synchrotron flux intensity evaluated at 1 GHz, $\alpha_{\rm syn}$ the synchrotron spectral index (for flux units) and Ω the solid angle covered.

3.1.2 Free–free emission

Unlike synchrotron, free–free emission is radiated by electrons accelerated by electric fields (e.g. Rybicki & Lightman 1979; Condon & Ransom 2016). Its almost flat spectrum implies that it can be important at both low (below 10 GHz) and medium (between 10 and 100 GHz) frequencies. Because of this, important degeneracies between the free–free and other components (mostly AME and synchrotron) can arise. A function of the absorption along the line of sight, or opacity, $\tau_{\rm ff}$, is needed to describe free–free. We use the parametrization from Draine (2011):

$$S_\nu^{\rm ff}({\rm EM}) = \frac{2k_{\rm B}\nu^2}{c^2}\Omega T_{\rm ff} \tag{3}$$

with

$$T_{\rm ff} = T_{\rm e}\left(1 - {\rm e}^{-\tau_{\rm ff}}\right)$$
$$\tau_{\rm ff} = 5.468 \cdot 10^{-2} \cdot \left(\frac{\rm EM}{\rm pc\ cm^{-6}}\right) \cdot \left(\frac{T_{\rm e}}{\rm K}\right)^{-3/2} \cdot \left(\frac{\nu}{\rm GHz}\right)^{-2} \cdot g_{\rm ff}(\nu)$$
$$g_{\rm ff}(\nu) = \ln\left[\exp\left(5.960 - \frac{\sqrt{3}}{\pi}\cdot \ln\left[\frac{\nu}{\rm GHz}\left(\frac{T_{\rm e}}{10^4\ {\rm K}}\right)^{-3/2}\right]\right) + {\rm e}\right],$$

where we take only the emission measure, EM, as a free parameter. The electron temperature, on the other hand, is fixed at $T_{\rm e} = 8000$ K[6] (as in e.g. Planck Collaboration 2011; Génova-Santos et al. 2015). This component dominates over synchrotron as the frequency increases. There are few data studying diffuse emission at frequencies between 3 and 10 GHz (because of the need for large telescopes), where we expect synchrotron and free–free to overlap, so both are usually strongly degenerate. However, current and future experiments will help solve this issue (Irfan et al. 2015; Cepeda-Arroita et al. 2021).

3.1.3 AME

The physical processes responsible for AME are not clear yet. Even though limits on polarization (López-Caraballo et al. 2011; Génova-Santos et al. 2015; Tramonte et al. 2023) partly discard the possibility of a magnetic origin, it is still not clear whether they are linked to PAHs or not (Hensley et al. 2016; Dickinson et al. 2018; Ysard et al. 2022). Theoretical models for the electric dipole emission from spinning dust depend on a large number of parameters (Ali-Haïmoud et al. 2009; Silsbee, Ali-Haïmoud & Hirata 2011), so we chose instead to use a simpler, phenomenological model. This model consists of a log-normal distribution, which mimics well enough the spinning dust models (Stevenson 2014; Cepeda-Arroita et al. 2021; Poidevin et al. 2023):

$$S_\nu^{\rm AME}(I_{\rm AME}, \nu_{\rm AME}, W_{\rm AME}) = I_{\rm AME}\ \exp\left[-\frac{1}{2W_{\rm AME}{}^2}\ln^2\left(\frac{\nu}{\nu_{\rm AME}}\right)\right]\Omega, \tag{4}$$

where $I_{\rm AME}$ is the maximum flux intensity due to AME, $\nu_{\rm AME}$ the correspondent frequency for that maximum, and $W_{\rm AME}$ the width of the distribution on the log-log plane.

3.1.4 Dust emission

Thermal dust dominates the spectrum at higher frequencies, and we fitted its emission to a single modified blackbody (MBB):

$$S_\nu^{\rm dust}(\tau_{353}, \beta_{\rm d}, T_{\rm d}) = \frac{2h\nu^3}{c^2}\left(\frac{\nu}{353\ {\rm GHz}}\right)^{\beta_{\rm d}} \tau_{353}\frac{1}{{\rm e}^x - 1}\Omega, \tag{5}$$

where τ_{353} is the optical depth normalized at 353 GHz, $\beta_{\rm d}$ is the dust emissivity and $x = h\nu/k_{\rm B}T_{\rm d}$, with $T_{\rm d}$ being the dust temperature.

3.1.5 CMB

Finally, we accounted for a contribution from CMB anisotropies in our photometry method. We estimated the flux density from CMB anisotropies as:

$$\Delta S_\nu^{\rm CMB}(\Delta T_{\rm CMB}) = \frac{2k_{\rm B}\nu^2}{c^2}\frac{x^2{\rm e}^x}{({\rm e}^x - 1)^2}\Delta T_{\rm CMB}\Omega, \tag{6}$$

where $x = h\nu/k_{\rm B}T_{\rm CMB}$ and $\Delta T_{\rm CMB}$ models the CMB anisotropies. $T_{\rm CMB}$ is fixed to 2.72548 K (Fixsen 2009). In this study, the amplitude of this CMB component was consistent with the expected value at these angular scales (80 µK). This value makes the CMB less bright than the rest of components.

3.2 Estimation of flux densities for individual pixels

We built a SED between 0.408 and 3000 GHz for each HEALPIX $N_{\rm side} = 64$ pixel in the region described in Section 2. The flux densities for each pixel were computed only for the maps listed in Table 1 that covered that pixel (e.g. pixels with $\delta > 0^\circ$ did not have data from the Jonas et al. 1998 survey, for example). These flux densities were calculated by subtracting the signal from an aperture outside the Galactic plane (the so-called zero-level reference aperture, see below) from the signal from each pixel aperture, which accounts only for the pixel itself:

$$S_\nu = a(\nu)\Omega T = \frac{2k_{\rm B}\nu^2}{c^2}\frac{x^2{\rm e}^x}{({\rm e}^x - 1)^2}\Omega T, \tag{7}$$

where S_ν is the flux density at frequency ν, $a(\nu)$ is the conversion factor between thermodynamic temperature and intensity, $x = h\nu/k_{\rm B}T_{\rm CMB}$, and Ω is the solid angle covered by a single pixel. T is the difference between the temperature in the pixel we want to study, $T_{\rm aper}$, and the median temperature in the zero-level reference region, ${\rm med}(T_{\rm BG})$: $T = T_{\rm aper} - {\rm med}(T_{\rm BG})$. This zero-level reference region is defined here as a 1 degree radius aperture outside the Galactic plane and centred on (RA, δ) = (157.5°, +8°). Its uncertainty (σ) is estimated as the quadratic sum of the statistical and calibration uncertainties (the latter can be checked in Table 1), as in the following equations (Rubiño-Martín et al. 2012; Génova-Santos et al. 2015):

$$\sigma_{\rm AP} = a(\nu)\Omega\,\sigma(T_{\rm BG})\sqrt{\frac{1}{n_{\rm aper}} + \frac{\pi}{2}\frac{1}{n_{\rm BG}}} \tag{8}$$

---

[6] The selection of $T_{\rm e}$ is not relevant, as it is importantly degenerated with *EM* and does not have a significant effect on the shape of the spectrum. Thus, only one of the two are needed to fix the amplitude.

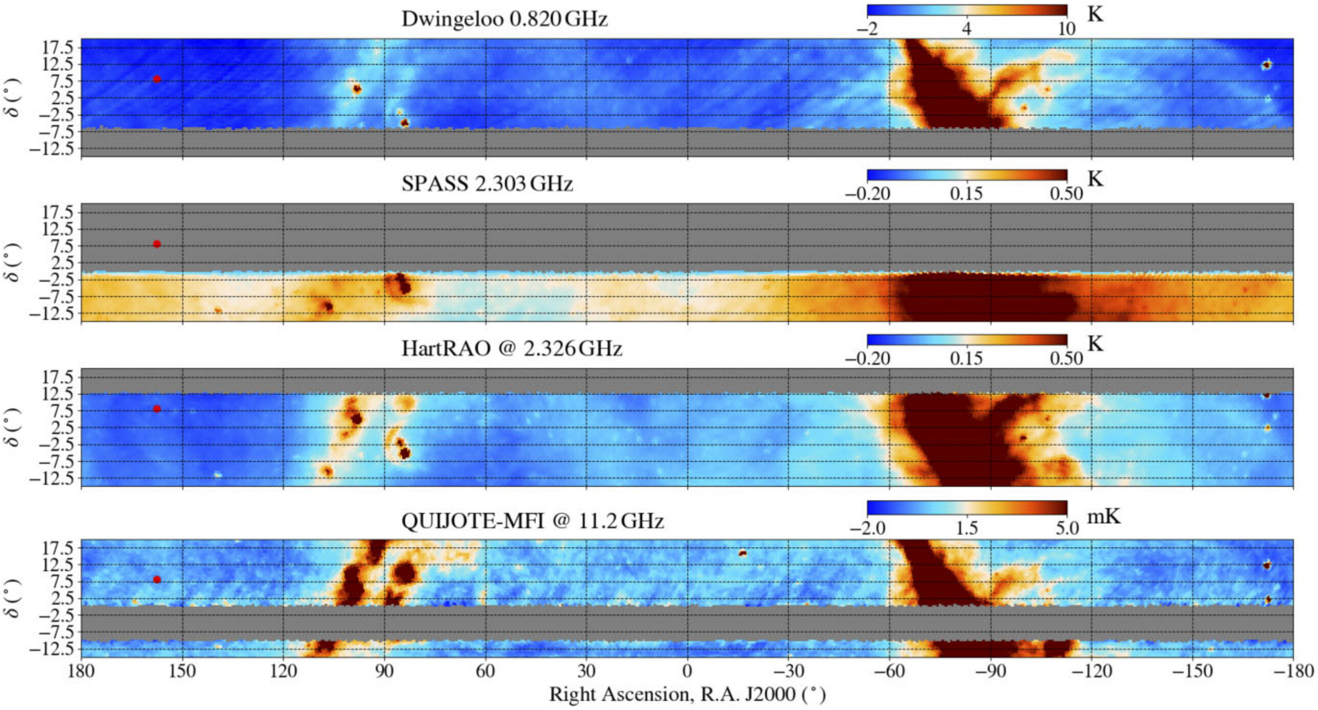

Figure 2. Equatorial view of the overlapping region between Berkhuijsen (1972), Jonas et al. (1998) and 11.2–12.9 GHz bands from QUIJOTE-MFI surveys ($0^\circ < \delta < 13^\circ$). The background region pixels, which defined the map zero-levels for the analyses, are those within the red dot at (RA, δ) = (157.5°, +8°). This region was selected in an effort to avoid regions with high emission in the lower frequency surveys. It should also be as far as possible from both the satellite band ($-10^\circ < \delta < 0^\circ$) and the upper declination Jonas et al. (1998) survey limit. SPASS (Carretti et al. 2019) map is also shown, for comparison.

$$\sigma_{S_\nu} = \sqrt{\sigma_{\rm AP}^2 + {\rm cal}^2 \cdot S_\nu^2}, \tag{9}$$

where $n_{\rm aper}$ and $n_{\rm BG}$ are the number of pixels embedded in each aperture, constant, and equal to 1 and 11 pixels, respectively, and $\sigma(T_{\rm BG})$ is the temperature standard deviation within the background aperture. This way of estimating uncertainties is conservative, as we are assuming calibration errors to be uncorrelated across frequencies, which is not true.

It is worth noting that although we keep the notation from aperture photometry works, we did not perform a standard aperture photometry analysis where a background region is selected to correct for the local background emission. Instead, we used a common region for all pixels to define a reference zero level for the whole Galactic plane (as in, for example, Planck Collaboration 2014c). Determining zero-levels in radio surveys is a critical step for component separation analyses (Wehus et al. 2017), and these are especially difficult to define for the low-frequency (<10 GHz) surveys used in this work. Besides, after applying the FDEC filtering to the QUIJOTE-MFI data (as explained in Section 2.4), some power at large angular scales is removed from the maps, and in particular, the mean levels of the maps are removed. For our analysis, all ancillary maps are filtered using the same FDEC approach as for QUIJOTE-MFI. The selection of a common aperture to set the new (common) zero level of all maps is thus needed for a consistent analysis. This reference background region must be present in all maps, so it should be in the overlapping region $0^\circ < \delta < 13^\circ$ between Berkhuijsen (1972), Jonas et al. (1998) and the 11.2–12.9 GHz QUIJOTE surveys (Fig. 2). We selected the aperture with radius $r = 1^\circ$ located at $\delta = 8^\circ$ that minimized WMAP *K*-band flux, as this band is one of the best AME detection proxies. This aperture is located at RA = 157.5°. We tested several apertures with fixed $\delta = 8^\circ$ and variable RA, and none of them introduced biases greater than 1 Jy on the WMAP K band map. We did the same for *Planck-HFI* 143 and 353 GHz bands to show that the region selection was not biasing the thermal dust calculation. We found that there were no regions without evident emission from Galactic structures that had a median value further than 1σ away from the value obtained from our chosen background region. This σ is calculated as the quadratic sum of the uncertainties from both our chosen aperture and the tested ones. Therefore, our method is robust against changes when choosing the background region, maintaining the following results.

Finally, we ran several tests applying variations to the zero-levels of the flux density values from the low frequency surveys compatible with their photometric uncertainties. These are mostly dominated by calibration uncertainties, which are conservatively defined. We found that the distributions for the AME parameters are not affected by these changes on the zero-levels. $I_{\rm AME}$ median values from the marginalized posteriors were less than $\pm 0.1\sigma$ away from their real values, where σ is computed as the quadratic sum of the dispersions from the real and simulated cases. The effect was slightly larger for $\nu_{\rm AME}$, but still under $\pm 0.2\sigma$, while negligible for $W_{\rm AME}$. On the other hand, the changes for $I_{1\,{\rm GHz}}$ could be as important as $\pm 0.6\sigma$. This proved that our results on AME are robust against variations in the zero-levels of the low-frequency surveys.

3.2.1 *QUIJOTE data uncertainties assessment*

Classical aperture photometry studies (from the QUIJOTE collaboration Génova-Santos et al. 2015, 2017; Poidevin et al. 2019 and previous experiments – e.g. Planck Collaboration 2014b) estimated the aperture flux density uncertainty as described above by using the scatter between pixels in the background aperture. In that case,

Table 2. Top-hat priors for the parameters during the MCMC. Please notice that we are referring to the synchrotron spectral index, $\alpha_{\rm syn}$, in flux density, not in temperature ($\beta_{\rm syn} = \alpha_{\rm syn} - 2$).

Parameter	Lower prior	Upper prior
$I_{1\,\rm GHz}$ (Jy sr^{-1})	0	—
$\alpha_{\rm syn}$	−2	1
EM (pc cm^{-6})	1	—
$I_{\rm AME}$ (Jy sr^{-1})	0	—
$\nu_{\rm AME}$ (GHz)	10	60
$W_{\rm AME}$	0.2	1
τ_{353}	0	—
$\beta_{\rm d}$	0	3
$T_{\rm d}$ (K)	10	40
$\Delta T_{\rm CMB}$ (μK)	−600	600

we rely on the assumption that the background fluctuation level is similar between the aperture and the background regions. However, we found large-scale residuals due to 1/*f* in the QUIJOTE-MFI intensity maps (particularly at 17 and 19 GHz), which implied that this assumption might not be correct for that data set. This is especially severe for this kind of analysis, where the aperture and background regions are far apart. We therefore generated a set of $N = 1000$ simulations for the QUIJOTE-MFI bands to quantify the correlated noise plus instrumental and systematic effects. Further description of these noise simulations is provided in Section 6 of Rubiño-Martín et al. (2023). We used the simulations to compute an additional contribution to the aperture photometry uncertainty to account for large-scale variations between parts of the maps:

$$\sigma_{\rm sims} = \sqrt{\sum_{i}^{N} \frac{(S_{0+i} - S_0)^2}{N}}, \tag{10}$$

where S_0 is the aperture flux density computed on the QUIJOTE-MFI map alone, and S_{0+i} is the same result when the i-sm simulation is added to that QUIJOTE-MFI map. Statistical and calibration uncertainties still needed to be added quadratically when using this estimator. Thus, the final uncertainty estimates for QUIJOTE-MFI flux densities[7] increased from that described in equation (9) to:

$$\sigma_{S_\nu} = \sqrt{\sigma_{\rm AP}^2 + \sigma_{\rm sims}^2 + {\rm cal}^2 \cdot S_\nu^2}. \tag{11}$$

3.3 SED fitting through MCMC

For each pixel, we used a Maximum Likelihood Estimator (MLE) to obtain the posterior distribution for the (10) free parameters described in Section 3.1:

$$\theta = (I_{1\,\rm GHz},\ \alpha_{\rm syn},\ {\rm EM},\ I_{\rm AME},\ \nu_{\rm AME},\ W_{\rm AME}, \tau_{353},\ \beta_{\rm d},\ T_{\rm d},\ \Delta T_{\rm CMB}).$$

We apply flat priors on these parameters, which are listed in Table 2. These are defined to be as little restrictive as possible. χ^2 depends on the sum of the differences between measured, $\boldsymbol{S}$, and expected, $\boldsymbol{S}^{\rm total}(\theta)$, flux densities across the frequency domain, and their covariance, $\boldsymbol{C}$:

$$\chi^2 = (\boldsymbol{S} - \boldsymbol{S}^{\rm total}(\theta))^{\rm T} \boldsymbol{C}^{-1} (\boldsymbol{S} - \boldsymbol{S}^{\rm total}(\theta)). \tag{12}$$

When every combination of surveys has negligible covariance, the previous equation turns into:

$$\chi^2 = \sum_{\nu} \left[\frac{S_\nu - S_\nu^{\rm total}(\theta)}{\sigma_{S_\nu}} \right]^2,$$

where the measured flux density (S_ν) and its uncertainty (σ_{S_ν}) are obtained through aperture photometry, as described in equations (7) and (11). However, QUIJOTE-MFI frequencies observed by the same horn (11.2–12.9 GHz and 16.8–18.7 GHz) are highly correlated, so this assumption is no longer valid. The required correction will be explained in Section 3.3.1.

We therefore built a log-likelihood MLE using χ^2 from equation (12):

$$\log \mathcal{L} = -0.5 \cdot \chi^2 = -0.5 \cdot \left(\boldsymbol{S} - \frac{\boldsymbol{S}^{\rm total}(\theta)}{\boldsymbol{cc}} \right)^{\rm T} \boldsymbol{C}^{-1} \left(\boldsymbol{S} - \frac{\boldsymbol{S}^{\rm total}(\theta)}{\boldsymbol{cc}} \right), \tag{13}$$

where $\boldsymbol{cc}$ accounts for the required colour corrections to be applied to the surveys. Colour corrections must be applied to account for the fact that the measured flux densities are integrated on the bandpass of each experiment detector and are explained in Section 3.3.2. This log-likelihood is used within the MCMC sampler ensemble from the EMCEE package (Foreman-Mackey et al. 2013).

The initial values for the fit parameters were drawn from the respective COMMANDER (PL16; downgraded to $N_{\rm side} = 64$) pixel posteriors. We then ran the chains to build the posteriors using the priors in Table 2 until they converged. We produced an additional set of results by adding a Jeffrey's ignorance prior (e.g. Eriksen et al. 2008) to prevent $\alpha_{\rm syn}$ parameter from being biased towards steeper values: however, the differences with our results were compatible within our uncertainties. We relied on the autocorrelation time from the EMCEE sampler to assess whether convergence had been achieved, so the number of required chain steps changes from pixel to pixel. This issue is further discussed in Appendix B. Once convergence was achieved, we recovered the median value from the parameter posteriors as their final value. Their uncertainties were estimated as half the difference between their 84th and 16th percentiles.

An example SED computed with this method can be seen in Fig. 3, where the fit was obtained as the sum of all the components described in Section 3.1. This is a pixel dominated by AME, with more than 50 per cent of its flux density between 20 and 30 GHz coming from that component. It is clearly visible how the spectrum rises at QUIJOTE-MFI lower frequencies due to AME. There are no large residuals across the full frequency domain, the largest one being the one from the WMAP *K* band because of its low uncertainty.

The corner plot showing the parameter posteriors obtained for this pixel is shown in Fig. 4, where some degeneracies are clearly visible. The most important ones are those involving the synchrotron ($I_{1\,\rm GHz}$), free–free (EM), and AME ($I_{\rm AME}$) amplitudes. The synchrotron index, $\alpha_{\rm syn}$, is also correlated with EM. The degeneracies between the dust parameters are well-known, especially that between $\beta_{\rm d}$ and $T_{\rm d}$ (e.g. Planck Collaboration 2014a). These behaviours are common for most of the pixels in this study; it is also usual that EM is the worst defined parameter. This was expected, owing to the flat free–free behaviour, which makes it strongly degenerate with both the synchrotron emission and AME.

To validate our fitting procedure and to show that we produced unbiased estimates for the various parameters, we generated synthetic SEDs for the pixel shown in Figs 3 and 4. We built a multivariate Gaussian distribution taking into account the flux density values

---

[7] The rest remain as in equation (9).

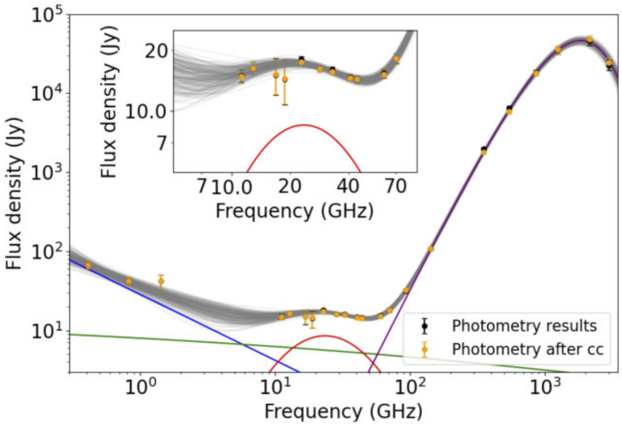

Figure 3. Example of a SED for one pixel – the one centred on $(l, b) = (111.1^\circ, 3^\circ)$ specifically. Photometry values are plotted twice: before and after applying their colour corrections. The embedded panel shows in detail the region where AME dominates over the rest of foregrounds. Random realizations from the MCMC are also shown in grey. It is clear that there is a larger dispersion for the fitted models between 1 and 10 GHz, where the degeneracy between synchrotron and free–free appears. The foreground component SEDs defined by their median parameter values (from Fig. 4) are also displayed.

obtained using aperture photometry, S_ν, and the full covariance, $\boldsymbol{C}$. We took random guesses from this distribution, building a simulated set of flux densities, $S_\nu^{\rm sim}$. We then ran the MCMC and fitted the SED formed by these simulated flux densities in the same way as described before in this section for the real data, and checked whether the results had changed. We found no such variations: when combining the parameter posteriors obtained from all the simulated SEDs, we recovered the same posteriors as when directly studying the real pixel SED.

The complete final maps took ≃10 700 (more than 1.2 years) hours of CPU time to compute the parameter posteriors for the 5309 independent pixels. We used the HTCONDOR distributed system at the IAC: the median and standard deviation computation times were $1.66^{+1.04}_{-0.46}$ hours for each pixel.

3.3.1 *Correlations between pairs of frequencies*

As previously stated in Section 2.1 of Rubiño-Martín et al. (2023), frequencies obtained with the same horns from QUIJOTE, i.e. 11.2–12.9 GHz and 16.8–18.7 GHz, are highly correlated in intensity (up to 80 per cent). Thus, those pairs of points could not be taken as independent when building the SED, so the covariance matrix was no longer diagonal when calculating χ^2 for the likelihood estimate. The covariance matrix components were then defined by the following equation:

$$c_{ij} = (\rho_{ij} + \delta_{ij})\sigma_i\sigma_j \tag{14}$$

where $\delta_{\rm ij}$ is the Kronecker delta and

$$\rho_{ij} = \begin{cases} 0.8 & (i, j) \mid (j, i) = 11.2,\ 12.9\,\text{GHz} \\ 0.8 & (i, j) \mid (j, i) = 16.8,\ 18.7\,\text{GHz} \\ 0 & \text{otherwise} \end{cases} \tag{15}$$

3.3.2 *Colour corrections*

Colour corrections (cc) were performed iteratively through the MCMC for every point above 10 GHz: QUIJOTE-MFI, WMAP, *Planck-LFI* and *HFI* and COBE-DIRBE experiments. It was assumed to be unnecessary for lower frequency surveys owing to their narrower bandpasses. Depending on the frequency point studied, one of two approximation methods was used:

(i) Frequencies below 100 GHz: we used a power law approximation where, for each frequency (ν) a spectral index (α_ν) was obtained while assuming $S_\nu^{\rm total}(\theta)$ was linear in its log-log space vicinity. As the colour correction was embedded inside the MCMC and computed every time we performed a step, reducing the computation time was critical. That is why we produced a second-order polynomial fit, tabulating the colour correction, *cc*, as a function of the spectral index, α_ν. This was done for every experiment before running the MCMC. For every step of the MCMC, we computed α_ν, and re-scaled the flux densities obtained from aperture photometry with the appropiate $cc(\alpha_\nu)$. This was done using FASTCC (Peel et al. 2022), as explained in Rubiño-Martín et al. (2023).

(ii) For frequencies above 100 GHz, where the thermal dust emission dominates the SED, the former approximation was no longer valid, as spectra had a more pronounced curvature and bandwidths were larger. We switched to a greybody model described by the thermal dust index and temperature, $cc(\beta_{\rm d}, T_{\rm d})$. This implied that we had to built 2D grids to tabulate *cc* values against $\beta_{\rm d}$ and $T_{\rm d}$, instead of having a polynomial fit that could be evaluated at a certain value, as happened for $cc(\alpha_\nu)$ for frequencies below 100 GHz. Within the MCMC, we then took the appropriate $cc(\beta_{\rm d}, T_{\rm d})$ factor from the grid taking into account the value of $\beta_{\rm d}$ and $T_{\rm d}$ on each step of the MCMC and re-scaled the flux density estimate accordingly.

Normally, these $cc(\alpha)$ and $cc(\beta_{\rm d}, T_{\rm d})$ factors should multiply the flux densities obtained from aperture photometry. However, that would imply applying the factors also to re-scale the respective uncertainties. To avoid doing so, we introduced the colour-corrections to the likelihood calculation dividing the estimated flux density instead. This is already applied in equation (13).

4 RESULTS

The five emission components considered (synchrotron, free–free, AME, thermal dust, and CMB anisotropies) are defined by 10 parameters, $\theta = (I_{1\,\rm GHz}, \alpha_{\rm syn}, {\rm EM}, I_{\rm AME}, \nu_{\rm AME}, W_{\rm AME}, \tau_{353}, \beta_{\rm d}, T_{\rm d}, \Delta T_{\rm CMB})$, as explained in Section 3.1. The maps for these parameters are shown in Fig. 5. For some of the analyses, we discarded pixels with $\mathrm{SNR}_{\rm AME} = I_{\rm AME}/\sigma(I_{\rm AME}) < 2$, as AME is the emission component we are mainly interested in. We have also applied a $\mathrm{SNR}_{\rm AME} < 3$ threshold and seen that the results do not change between the two cases. Thus, keeping $\mathrm{SNR}_{\rm AME} > 2$ allows us to increase the sample (by almost a factor 3) while maintaining the results. Moreover, in this way we prevent the presence of a positive $I_{\rm AME}$ bias from pixels with no AME emission. The previous maps with those pixels masked are shown in Appendix C. We also masked the pixels located less than 1.5° away from the SIMBAD[8] positions of Tau A, Cas A, and Cyg A.

None of the priors introduced in Section 3 was too restrictive according to the posterior distributions for the parameters. This

---

[8] http://simbad.u-strasbg.fr/simbad/ (Wenger et al. 2000)

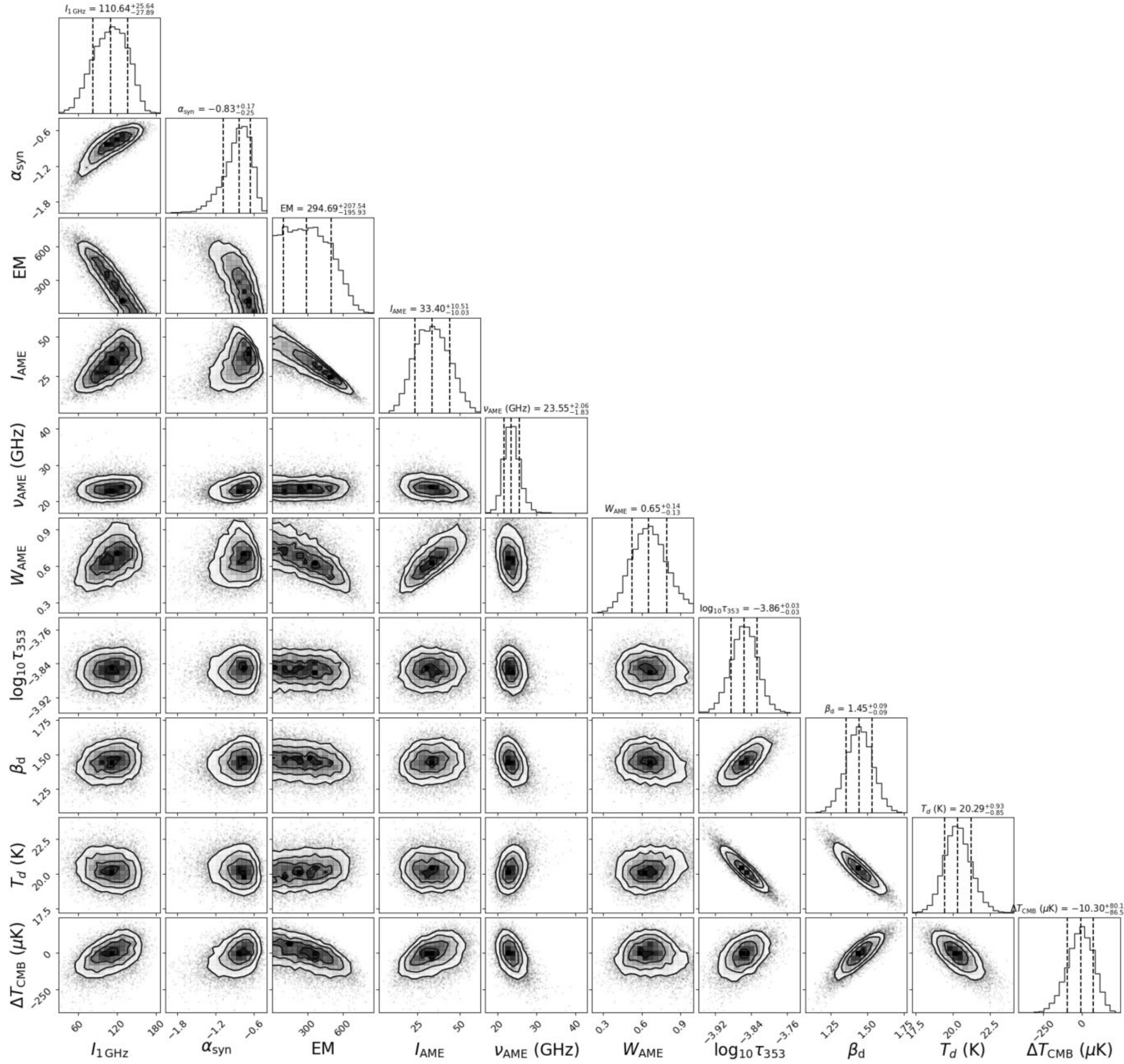

Figure 4. Corner plot containing the marginalized posteriors and correlation plots for the parameters describing the SED from Fig. 3. Their median and 16th and 84th percentile values are plotted with vertical dashed lines in the 1D marginalized posteriors: final parameter values and their uncertainties are obtained from those values. In the case of asymmetric distributions, such as the one for $\alpha_{\rm syn}$, there is a displacement between the median and the peak of the posterior. We see degeneracies that are common for most of the pixels in the map, mainly those between synchrotron, free–free and AME amplitudes ($I_{1\,\rm GHz}$, EM, $I_{\rm AME}$) or the dust parameters (especially $\beta_{\rm d}$ and $T_{\rm d}$). $I_{1\,\rm GHz}$ and $I_{\rm AME}$ units are 10^3 Jy sr^{-1}, while *EM* units are pc cm^{-6}.

is demonstrated in Fig. 4, where it is seen that in most cases the 95 per cent confidence intervals of the 2D posteriors lie well within the flat priors. In the opposite scenario, we would expect to have the peak of the posterior close to any of the flat prior edges.[9] For example, $W_{\rm AME}$ is one of the most complex parameter to constrain: small inconsistencies between adjacent flux densities in the SED can be compensated by a really narrow AME component, so $W_{\rm AME}$ would be biased to low values. Also, large $W_{\rm AME}$ values turn the spinning dust contribution almost into a power-law in the 10–60 GHz domain, so it would be replacing free–free. However, $W_{\rm AME}$ has median values between 0.4 and 0.8 for almost every pixel, while the lower and upper priors were 0.2 and 1, avoiding any of the previous possible issues.

Apart from studying the pixel set presented in Section 2 in its entirety, we defined a series of regions to be studied independently, which we named ‘sectors’. The first two correspond to regions with different data information, while Sectors 3–6 study various galactic longitude cuts:

(i) Sector 1: $\delta < -10^\circ$. This covers the area below the QUIJOTE satellite band at low longitudes, i.e. the Galactic Centre and the pixels located at $l \simeq -120^\circ$. For this region we have no data from the

---

[9] This happens for the EM in those pixels where the free–free emission is not large, but EM > 0 is a physical prior, as emission cannot be negative.

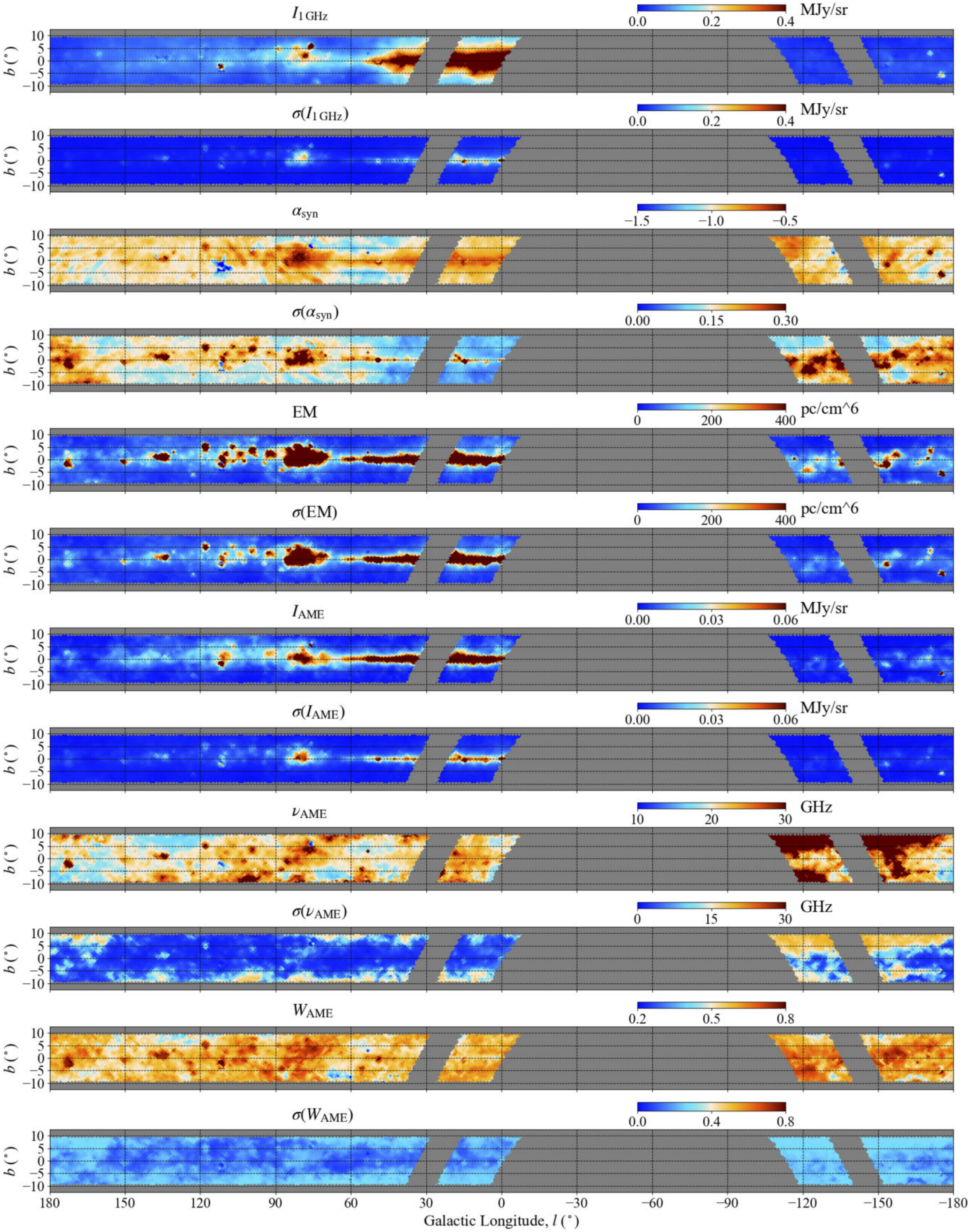

Figure 5. Reconstructed maps for the parameters describing synchrotron, free–free, and AME. We can see how the α_{syn} uncertainty decreases for the band $\delta \in (0°, 13°)$, owing to the addition of a fourth point (from the Jonas et al. 1998 survey) to the low-frequency (0.4–3 GHz) regime. It is also clear how the EM uncertainties remain high for most of the pixels in the plane. Regarding the AME parameters, ν_{AME} and W_{AME} have high SNRs along the plane, and both decrease as we get farther from the plane.

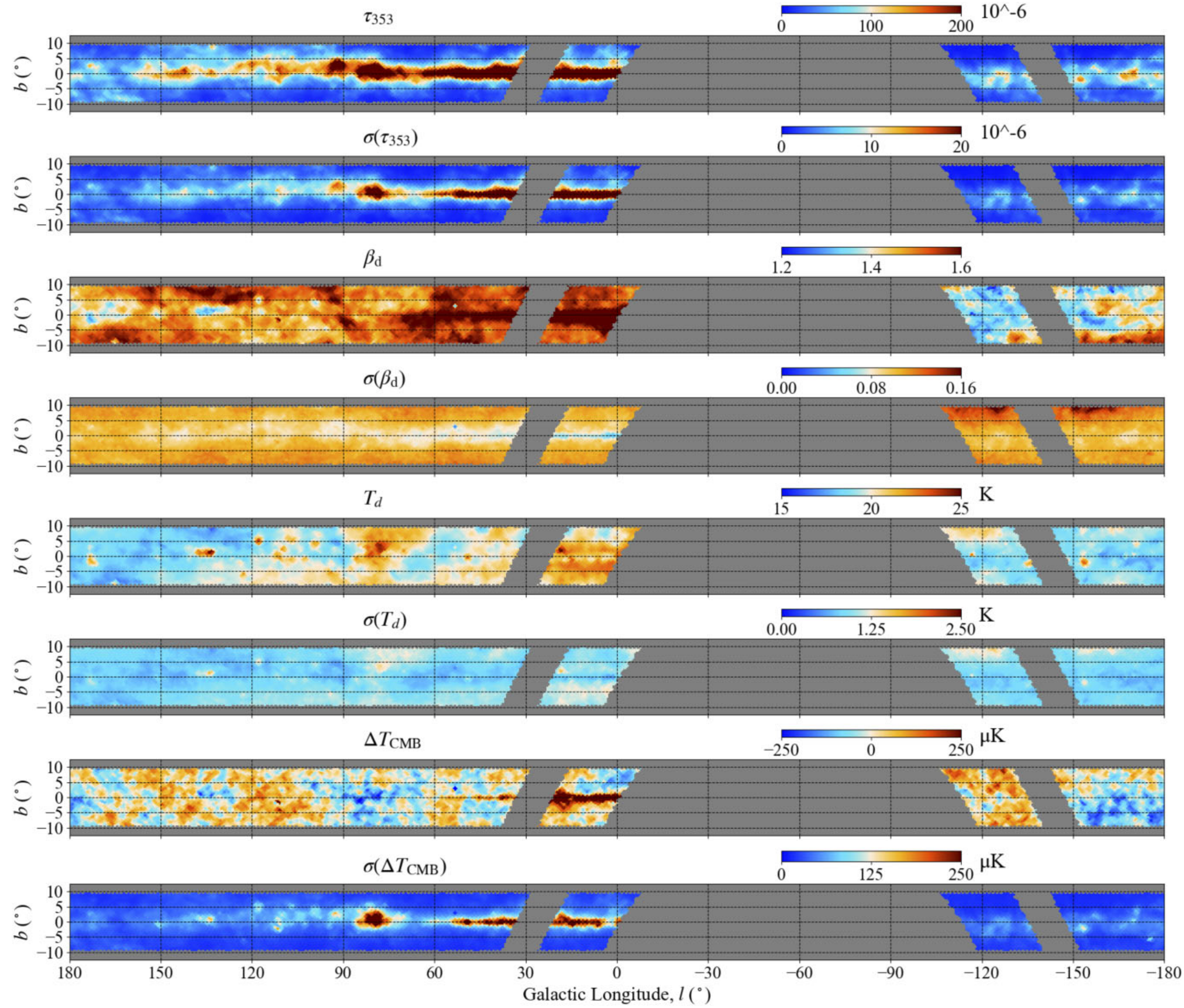

Figure 5. *(continued)* Reconstructed maps for the dust and CMB parameters. The colourbar limits for the dust parameters uncertainties have been fixed to 10 per cent of those for the parameters themselves. $\Delta T_{\rm CMB}$ shows a clear residual near the Galactic Centre, due to the model failing to reproduce all the measured flux density between 100 and 200 GHz with just one thermal dust component. The residual thermal dust emission is accounted for by the CMB component instead.

Dwingeloo survey at 0.820 GHz, but we do have data from HartRAO survey at 2.326 GHz.

(ii) Sector 2: $\delta > 13°$. This covers the area where we have the complementary configuration to Sector 1: we have data at 0.820 GHz, but not at 2.326 GHz.

(iii) Sector 3: $|l| < 50°$. This covers the Galactic Centre and some pixels above the satellite band. $l \simeq 50°$ is, approximately, the point where synchrotron emission begins to be less important (as shown in Fig. 5).

(iv) Sector 4: $50° \leq l < 90°$. This region hosts the feature with the highest $\mathrm{SNR}_{\rm AME}$ from all the plane, at $l \simeq 60°$, $b \in (-5°, 0°)$, as can be seen in Fig. C1. The Cygnus region, located at $l \simeq 80°$ and dominated by free–free, is also embedded in this region.

(v) Sector 5: $90° \leq l < 160°$. This region has the longest QUIJOTE-MFI integration time (as shown in the figures in appendix A of Rubiño-Martín et al. 2023).

(vi) Sector 6: $160° \leq l < 200°$. This area covers the Galactic anticentre, where the total emission is lower. This region has limited interest in this work (the number of pixels with $\mathrm{SNR}_{\rm AME} > 2$ is low).

4.1 Spatial variations for AME parameters

The distribution of the reconstructed maps for $\nu_{\rm AME}$ and $W_{\rm AME}$ is shown in Fig. 6. The median values are $\nu_{\rm AME} = 21.6^{+5.8}_{-2.6}$ GHz, $W_{\rm AME} = 0.591^{+0.070}_{-0.069}$, where upper and lower confidence intervals were obtained as half the difference between the distribution 84th and 16th percentiles. These boundaries account for the variation in the parameter values along the Galactic plane and are not related to the uncertainties for those same parameters from the individual pixels.

After discarding pixels with $\mathrm{SNR}_{\rm AME} < 2$, the previous values turn to $\nu_{\rm AME} = 20.7^{+2.0}_{-1.9}$ GHz and $W_{\rm AME} = 0.560^{+0.059}_{-0.050}$. When this

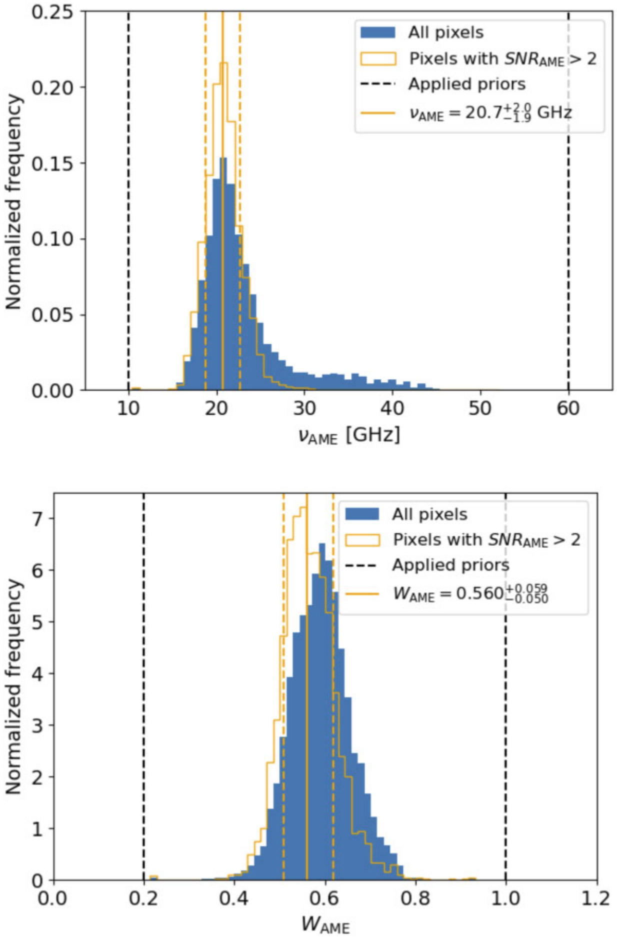

Figure 6. Top: distribution of $\nu_{\rm AME}$ values along the Galactic plane. We see that, when focusing on pixels with high $\rm SNR_{AME}$, the tail of pixels towards high $\nu_{\rm AME}$ values is suppressed. This greatly decreases the variability in the histogram (from $\nu_{\rm AME} = 21.6^{+5.8}_{-2.6}$ to $\nu_{\rm AME} = 20.7^{+2.0}_{-1.9}$). Bottom: distribution of $W_{\rm AME}$ values along the Galactic plane. The width of the distribution remains the same after removing those pixels with $\rm SNR_{AME} < 2$, but its median value decreases a little ($0.591^{+0.070}_{-0.069}$ versus $0.560^{+0.059}_{-0.050}$ from Tables 3 and 4). In both cases, the applied flat priors are shown as vertical dashed lines.

threshold is applied, the long tail towards high values of $\nu_{\rm AME}$ visible in Fig. 6 is suppressed. This last $\nu_{\rm AME}$ value is almost 2.5σ away from that obtained by the BEYONDPLANCK collaboration (Andersen et al. 2023), 25.3 ± 0.5 GHz, but that value was obtained as a joint fit for all sky pixels, and not just those with highest AME significance from the Galactic plane. Our median value is also lower than, but consistent with, that of Poidevin et al. (2023; hereafter, P23): 23.6 ± 3.6 GHz. Planck Collaboration (2014b; hereafter, PL14b) reported a weighted mean value of $\nu_{\rm AME} = 27.9$ GHz, slightly discrepant from the results mentioned above, but they lacked data between 2.3 and 22.8 GHz.[10] Therefore, in PL14b, they were unable to constrain both sides of the AME distribution, as we can do after the addition of QUIJOTE-MFI data. However, both works study compact Galactic sources, while our study is focused on the diffuse emission from the Galaxy. Harper et al. (2022) reported a consistent value of $\nu_{\rm AME} = 19.4 \pm 6.4$ GHz.

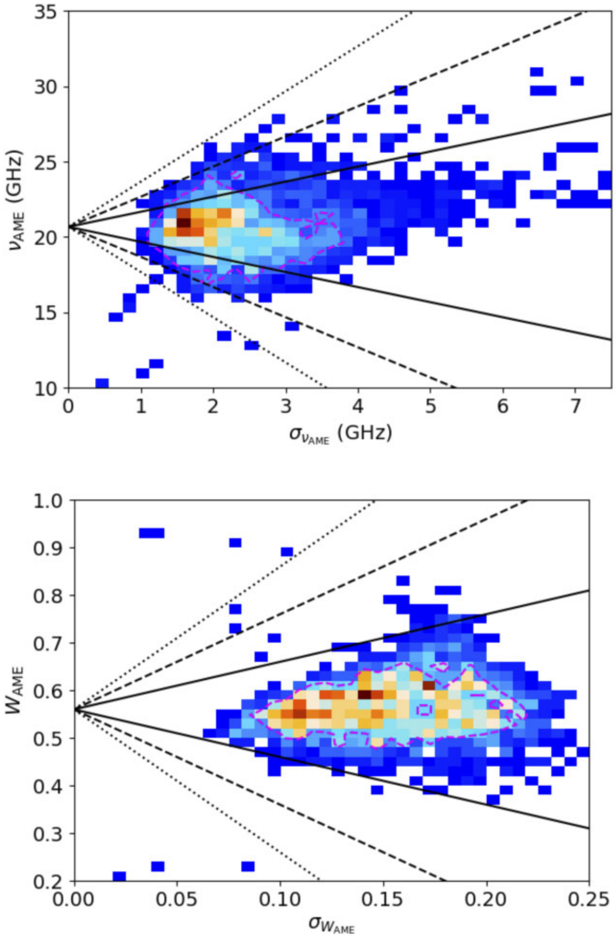

Figure 7. Spatial variations of $\nu_{\rm AME}$ and $W_{\rm AME}$ along the Galactic plane. The black lines show the median value of the distribution plus/minus 1 (solid), 2 (dashed), and 3 (pointed) times the dispersion from the parameter distribution (as shown in Fig. 6). Spatial variability is more important as more data are located outside the regions enclosed by those lines. We therefore see how the spatial variations along the Galactic plane are more important for $\nu_{\rm AME}$ than for $W_{\rm AME}$: the latter is, in fact, almost entirely embedded within 1σ (see text). Magenta lines enclose 68 per cent of the data. Both figures use just $\rm SNR_{AME} > 2$ pixels.

A log-normal AME distribution similar to the one used in this study was applied, although in that case the high-latitude sky was the focus of the study. This suggests that, on 1° scales, both studies could be most sensitive to AME at similar phases of the ISM. Rennie et al. (2022) studied a series of HII regions on arcminute scales and found $\nu_{\rm AME}$ values above 40 GHz, although with large (around 15 GHz) uncertainties.

We compared the dispersion of the parameters to their median value along the Galactic plane. Spatial variations are well detected for the intensity, $I_{\rm AME}$, with 66.4 per cent and 64.5 per cent (when the $\rm SNR_{AME} > 2$ threshold is applied) of the points showing residuals greater than 1σ. However, variations are not statistically significant for either $\nu_{\rm AME}$ or $W_{\rm AME}$ at 1 degree scales. This can be seen in Fig. 7, where we plot the results for $\rm SNR_{AME} > 2$ pixels versus their uncertainty and compare with the 1σ, 2σ, and 3σ variation levels. Only 17.9 per cent and 22.9 per cent of the pixels show differences greater than 1σ for $\nu_{\rm AME}$ when all pixels and just those with $\rm SNR_{AME} > 2$ are considered, respectively. These two values decrease even more, down to 1.5 per cent and 1.6 per cent, for $W_{\rm AME}$.

---

[10] However, the methodology was similar to the one in this study, as the AME was fitted with a single distribution. This distribution was obtained using `SPDUST`, and then variations in amplitude and peak frequency were allowed, although the shape (thus, the width of the distribution) remained the same.

Table 3. Median values, plus their dispersion, for a selected group of parameters along the sectors described at the beginning of Section 4. Every pixel in our $|b| < 10^\circ$ maps is taken into account. We see variations mostly between the regions closest to the Galactic Centre ($\delta < -10^\circ$; $|l| < 50^\circ$) and the rest of the plane. Both the synchrotron and dust indices ($\alpha_{\rm syn}$, $\beta_{\rm d}$), and the dust temperature ($T_{\rm d}$) show a decreasing trend as we get farther from the Centre. Uncertainties in this table and in Table 4 account for the histogram dispersions, not errors of the mean.

Parameter	All pixels	Sector 1 ($\delta < -10^\circ$)	Sector 2 ($\delta > 13^\circ$)	Sector 3 ($\lvert l\rvert < 50^\circ$)	Sector 4 ($50^\circ \leq l < 90^\circ$)	Sector 5 ($90^\circ \leq l < 160^\circ$)	Sector 6 ($160^\circ \leq l < 200^\circ$)
$\alpha_{\rm syn}$	-0.94 ± 0.10	-0.88 ± 0.09	-0.96 ± 0.08	-0.90 ± 0.12	-0.94 ± 0.16	-0.95 ± 0.06	-0.97 ± 0.06
$\beta_{\rm d}$	1.49 ± 0.08	1.49 ± 0.12	1.49 ± 0.06	1.55 ± 0.06	1.52 ± 0.06	1.49 ± 0.05	1.44 ± 0.07
$T_{\rm d}$ (K)	19.37 ± 1.19	20.17 ± 1.52	19.20 ± 1.07	20.72 ± 1.03	20.10 ± 1.07	19.11 ± 0.95	18.54 ± 0.64
$\nu_{\rm AME}$ (GHz)	21.63 ± 3.68	23.54 ± 6.70	20.95 ± 2.76	21.61 ± 2.30	21.80 ± 2.94	20.72 ± 2.24	20.89 ± 3.56
$W_{\rm AME}$	0.59 ± 0.06	0.61 ± 0.06	0.58 ± 0.06	0.58 ± 0.05	0.59 ± 0.08	0.57 ± 0.06	0.60 ± 0.06
$I_{\rm AME}/S_{\rm total}^{\nu_{\rm AME}}$	0.35 ± 0.15	0.21 ± 0.11	0.41 ± 0.12	0.27 ± 0.12	0.42 ± 0.13	0.43 ± 0.11	0.38 ± 0.12
$I_{\rm AME}/S_{\rm total}^{28.4\,{\rm GHz}}$	0.34 ± 0.14	0.21 ± 0.10	0.39 ± 0.12	0.28 ± 0.12	0.41 ± 0.14	0.40 ± 0.11	0.36 ± 0.12
$I_{\rm AME}/S_{\rm ff}^{\nu_{\rm AME}}$	1.07 ± 0.58	0.70 ± 0.50	1.20 ± 0.58	1.18 ± 0.46	1.26 ± 0.69	1.40 ± 0.53	0.85 ± 0.34
$I_{\rm AME}/S_{\rm ff}^{28.4\,{\rm GHz}}$	0.90 ± 0.50	0.65 ± 0.44	1.01 ± 0.49	1.05 ± 0.40	1.14 ± 0.60	1.19 ± 0.48	0.72 ± 0.25
$\epsilon_{\rm AME}^{28.4\,{\rm GHz}}$ (μK MJy^{-1} sr)	8.84 ± 3.77	6.79 ± 2.48	10.12 ± 3.65	5.70 ± 2.28	8.84 ± 3.01	11.43 ± 3.58	9.95 ± 3.88

However, this does not mean that these parameters do not vary pixel to pixel; those variations could be smaller than the statistical uncertainty from our analysis. For $\nu_{\rm AME}$, because of the small span of frequency values (97 per cent of the pixels with ${\rm SNR}_{\rm AME} > 2$ have $\nu_{\rm AME}$ values between 15 and 25 GHz) and high uncertainties [92 per cent of the pixels with ${\rm SNR}_{\rm AME} > 2$ have $\sigma(\nu_{\rm AME})$ larger than 1.5 GHz], it is difficult to have low residual values. Reducing the uncertainties would improve the detection of variability; this could also be achieved by studying smaller, correlated regions, as did Cepeda-Arroita et al. (2021; hereafter, CA21), where less smooth variations can be present.

We also qualitatively compare these results with theoretically proposed models. The SPDUST software (Ali-Haïmoud et al. 2009; Silsbee et al. 2011) is commonly used to build spinning dust SEDs: we compared its models with a log-normal distribution. We found that those models obtained using typical parameter values tend to have width ($W_{\rm AME}$) values below 0.6. As mentioned before, the median $W_{\rm AME}$ value in our results is $0.560^{+0.059}_{-0.050}$ when only those pixels with ${\rm SNR}_{\rm AME} > 2$ are considered. Thus, almost 50 per cent of the pixels show values higher than this limit. We repeated our analysis by reducing our flat prior to $W_{\rm AME}$ within [0.2, 0.6] to see if the wider prior artificially increased the values for $W_{\rm AME}$. $W_{\rm AME}$ individual pixel posteriors continued to have median values close to 0.6, the new prior, thus invalidating it. These higher-than-expected $W_{\rm AME}$ values were also measured by P23 and CA21 for unresolved sources and the λOrionis ring, respectively. The latter is particularly significant, as the use of data from the C-Band All Sky Survey (C-BASS), plus the absence of synchrotron, provides a better description of free–free. This directly improves its disentangling from AME: $W_{\rm AME}$ is still greater, however, than 0.5 for most of the regions with high AME significance. These results suggest that it may be convenient to revisit theoretical AME models to investigate how they could predict wider spectra.

4.1.1 Other emission components

For the other components, we expect a spatial distribution of amplitudes resembling the maps normally used as tracers of each type of emission. The 0.408 GHz Haslam et al. (1982) map describes synchrotron, while free–free can be described both by Hα (Haffner et al. 2003; Finkbeiner 2003) or radio-recombination lines (RRLs) maps (Alves et al. 2010), the latter being less affected by extinction than the former.[11] Finally, thermal dust is commonly described by any of the *Planck* highest-frequency bands or by the Schlegel, Finkbeiner & Davis (1998) map. Thermal dust templates are sometimes used as templates for the AME, as both are expected to be highly spatially correlated (Draine & Lazarian 1998a, b). In fact, we can see that the Haslam et al. (1982) map at 0.408 GHz from Fig. 1 present a similar morphology to that of the $I_{1\,{\rm GHz}}$ map in Fig. 5. The same happens for the *Planck-HFI* map at 353 GHz from Fig. 1 and the τ_{353} map from Fig. 5. The τ_{353} map is also similar to the $I_{\rm AME}$ map of Fig. 5, supporting the presence of a correlation between the AME and thermal dust components. CMB anisotropies are hard to constrain on top of the Galactic plane emission, as the other components are much brighter. Thus, the recovered uncertainties for this parameter ($\Delta T_{\rm CMB}$) are large, as can be seen in the bottom panel of Fig. 5.

4.2 Parameter variations with longitude

Following Planck Collaboration (2015a), we studied the average value of spectral indices (and other parameters) in the sectors defined at the beginning of Section 4. The results are presented in Table 3 for the full pixel set. Higher (flatter) values for $\alpha_{\rm syn}$ are obtained for the regions closer to the Galactic Centre. There is also a decreasing trend for the dust index and temperature, $\beta_{\rm d}$ and $T_{\rm d}$, as we get farther from the Galactic Centre. These types of behaviour can be seen in Fig. 8.

Our $\beta_{\rm d}$ estimates are close to the $\beta_{\rm mm} = 1.60 \pm 0.06$ value obtained by Planck Collaboration (2014a) for the $l \in (20^\circ, 44^\circ)$, $b \in (-4^\circ, 4^\circ)$ region. This area coincides with that of the satellite band, so it is not observed by QUIJOTE-MFI, but the result is more similar to the value for Sector 3: 1.56 ± 0.06. $T_{\rm d}$ values are also comparable between the two studies; however, *Planck* was fitting for a bimodal distribution, with a break at 353 GHz. When performing further analyses, constant $T_{\rm d} = 19$ K and $\beta_{\rm mm} = 1.52$ values were assumed by Planck Collaboration (2014a), which are, in fact, very

---

[11] We have tested how well the full-sky Hα map from the Wisconsin H-alpha Mapper (Haffner et al. 2003) compares to both EM and $T_{\rm d}$ maps, as the three should be linked to star formation. We found low *SRCC* values of 0.45–0.55; however, the maps show similar morphologies on high free–free emission regions, such as the Cygnus region or clouds in $l \in (180^\circ, 240^\circ)$. This low SRCC value is probably an effect of uncorrected extinction in the Hα map. Nevertheless, we must bear in mind that *EM* is the worst defined parameter throughout the plane, with a significance lower than 2 for most of the pixels.

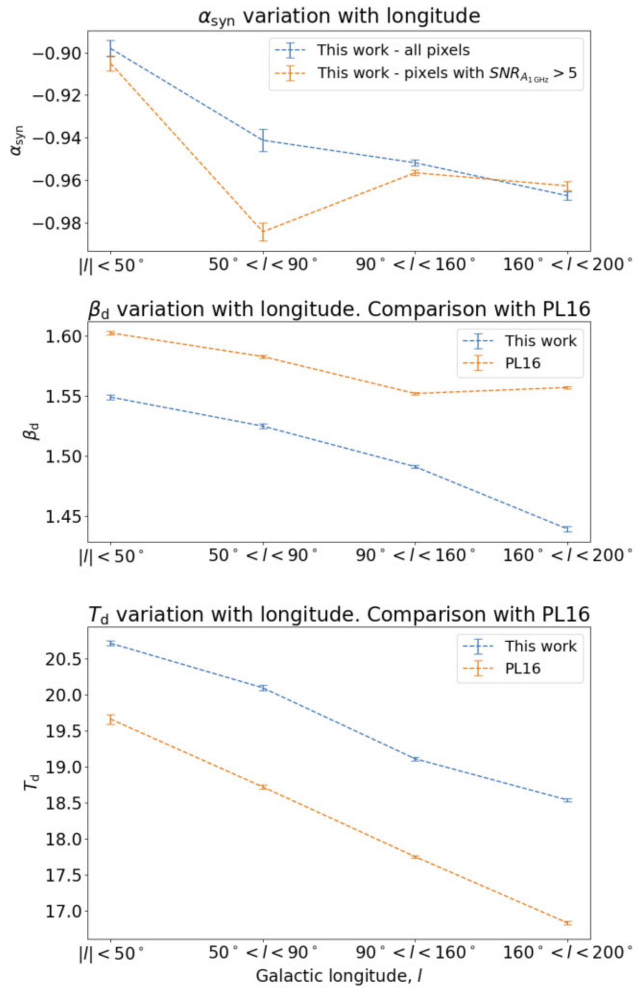

Figure 8. Top: variation of $\alpha_{\rm syn}$ along the regions described in Section 4. Middle: variation of $\beta_{\rm d}$ along the regions described in Section 4. Bottom: same as previous plot, but for $T_{\rm d}$. In all cases, we are plotting the error of the mean instead of the histogram variability (which is reported in Tables 3, 4, and 5): the difference between the two is a factor of $N_{\rm pix}^{-1/2}$. The values from COMMANDER code results described in PL16 are shown for comparison purposes.

close to our median results for the full plane (19.35 ± 1.23 K and 1.50 ± 0.09, respectively).The decrease in $\beta_{\rm d}$ values for $200^\circ < l < 240^\circ$ shown in Fig. 5 is also recovered in $\beta_{\rm d}$ maps from both Planck Collaboration (2014d, PL16), although in the latter case, the use of a strong prior on $\beta_{\rm d}$ reduces the amplitude of the decrement (see Section 5.3).

The ratio between AME and total flux densities at 28.4 GHz increases as we get farther from the Galactic Centre. This is also consistent with previous results. Planck Collaboration (2015a) focused on the regions with $|b| < 4^\circ$ and Galactic longitude in the ranges $l \in (20^\circ, 40^\circ)$ and $l \in (320^\circ, 340^\circ)$, and obtained $S^{28.4\,\rm GHz}_{\rm AME}/S^{28.4\,\rm GHz}_{\rm total} = 0.44 \pm 0.03$ on average, while in this work, we get 0.27 ± 0.12 for Sector 3 and 0.40 ± 0.14 for Sector 4. This last region is more adequate to be used as a reference for comparison because the first one contains the Galactic Centre. The AME to free–free emission ratio is also consistent but has a much higher uncertainty in our case: ≃1.0 ± 0.5 compared to the ≃0.85 ± 0.10 value from Planck Collaboration (2015a). These larger uncertainties are due to the wider latitude range in our study ($|b| < 10^\circ$ compared to $|b| < 4^\circ$), which translates into higher dispersion.

The AME emissivity is generally defined as the ratio between an AME tracer and a thermal dust one. Previous works used different parameters as tracers. In this study, we keep the notation from each of the papers we compare to. We show the variations along the Galactic plane for the ratio between the AME amplitude at 28.4 GHz and the COBE-DIRBE emission map at 100 μm, which we define as $\epsilon^{28.4\,\rm GHz}_{\rm AME}$. As both observables in the numerator and denominator depend on the column density, the emissivity cancels the density dependence, showing only sensitivity to the physics of the emission mechanism instead. The $\epsilon^{28.4\,\rm GHz}_{\rm AME}$ map is shown in the bottom panel of Fig. 9. We find $\epsilon^{28.4\,\rm GHz}_{\rm AME} = 11.62 \pm 3.45\,\mu{\rm K\,MJy^{-1}\,sr}$ when taking into account all pixels with $\rm SNR_{AME} > 2$. This estimate is consistent with the values of $10.9 \pm 1.1\,\mu{\rm K\,MJy^{-1}}$ sr of Davies et al. (2006; although in that case, $\epsilon_{\rm AME}$ referred to the 31 GHz WMAP *K* band), $9.8 \pm 0.5\,\mu{\rm K\,MJy^{-1}}$ sr of Planck Collaboration (2015a) and $14.0 \pm 3.5\,\mu{\rm K\,MJy^{-1}}$ sr of Harper et al. (2022). When focusing on variations with the longitude, it is clear that the Galactic Centre has a much lower $\epsilon^{28.4\,\rm GHz}_{\rm AME}$ than the rest of the plane.

Planck Collaboration (2016b) also showed how the emissivity changes in different regions and environments in the sky. The ratio between the AME amplitude at 22.8 GHz and τ_{353} was therefore used: we find $T^{22.8\,\rm GHz}_{\rm AME}/\tau_{353} = 9.84 \pm 3.57$ K for those pixels with $\rm SNR_{AME} > 2$. This value is really close to the high latitude ($|b| > 10^\circ$) cut from the previous Planck Collaboration (2016b), $T^{22.8\,\rm GHz}_{\rm AME}/\tau_{353} = 9.7 \pm 1.0$ K, and lower (but consistent, because of the large dispersion) to the value of $11.5^{+4.2}_{-1.5}$ K found by Harper et al. (2022). For the full sky, Planck Collaboration (2016b) found $T^{22.8\,\rm GHz}_{\rm AME}/\tau_{353} = 8.3 \pm 0.8$ K, which is also consistent with our result. At 30 GHz, we find $T^{30\,\rm GHz}_{\rm AME}/\tau_{353} = 4.66 \pm 2.18$ K, much lower than the value of 7.9 ± 2.6 K obtained at high latitudes by Hensley et al. (2016). At 28.4 GHz, the $T^{28.4\,\rm GHz}_{\rm AME}/\tau_{353} = 5.51 \pm 2.43$ K ratio is really similar to that of $5.8^{+2.9}_{-0.5}$ K obtained by Harper et al. (2022). The AME emissivity increment with Galactic longitude is more noticeable than for the AME fraction. But the difference between the anticentre (Sector 6) and the Centre (Sector 3) is still not statistically significant (just 1.75σ).

In Table 4, we show the same values as in Table 3 but only taking into account those pixels with high synchrotron, AME or dust significances, depending on the parameter studied. The results are similar to those for the whole pixel set, apart from a lower dispersion on AME parameter distributions and higher AME fraction when the $\rm SNR_{AME}$ threshold is introduced (as expected). There is also an inconsistency (2.9σ) for $\alpha_{\rm syn}$ in Sector 4 when introducing the $\rm SNR_{syn} > 5$ threshold (see Fig. 8). This is because for this region the threshold masks most of the pixels in the plane. These pixels come mainly from the Cygnus region, which is dominated by free–free emission (therefore their $\rm SNR_{syn}$ values are low). The weight of the pixels outside the Galactic plane (which in general show steeper values) for the determination of $\alpha_{\rm syn}$ is therefore higher.

4.3 Correlations between the model parameters

We have used the Spearman Rank Correlation Coefficient (hereafter, SRCC) to compare the correlations between parameters, as in PL14b, CA21, and P23. To maintain the notation of those articles, we have used the AME amplitude, $A_{\rm AME}$, instead of its intensity, $I_{\rm AME}$: $I_{\rm AME}$ was better for the representations on the maps. The relation between the two depends on the solid angle of our aperture (Ω), which is equal and constant to one $N_{\rm side} = 64$ pixel: $\Omega = 2.56 \times 10^{-4}$ sr . Some of the main correlations between the reconstructed parameters

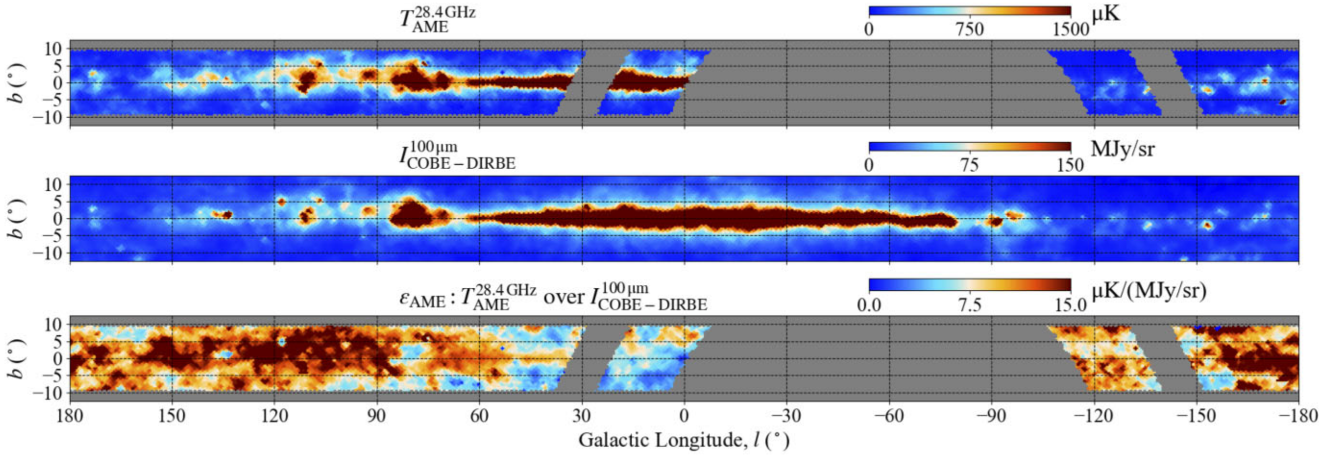

Figure 9. Top: map of the AME emission at 28.4 GHz. We have converted the map from intensity to temperature units to facilitate comparison with the literature. Middle: COBE-DIRBE map at 100 μm, showing thermal dust emission. Bottom: ratio between the former two, or AME emissivity. The values for the Galactic Centre are lower than in other areas and suggest that AME emission is much less efficient in that region.

Table 4. Similar to Table 3, but taking into account only pixels with $\mathrm{SNR_{syn}} = I_{1\,\rm GHz}/\sigma(I_{1\,\rm GHz}) > 5$ for $\alpha_{\rm syn}$, $\mathrm{SNR_{dust}} = \tau_{353}/\sigma(\tau_{353}) > 5$ for $\beta_{\rm d}$ and $T_{\rm d}$, and $\mathrm{SNR_{AME}} > 2$ for AME parameters, fractions and $\epsilon_{\rm AME}^{28.4\,\rm GHz}$. These selections account for 80 per cent, 100 per cent, and 47 per cent of the pixels, respectively, and are applied only to the corresponding component studied. The latter selection returns similar results as using $\mathrm{SNR_{AME}} > 3$, while increasing the sample.

Parameter	All pixels	Sector 1 ($\delta < -10°$)	Sector 2 ($\delta > 13°$)	Sector 3 ($\lvert l\rvert < 50°$)	Sector 4 ($50° \le l < 90°$)	Sector 5 ($90° \le l < 160°$)	Sector 6 ($160° \le l < 200°$)
$\alpha_{\rm syn}$	-0.94 ± 0.09	-0.88 ± 0.09	-0.96 ± 0.07	-0.90 ± 0.11	-0.98 ± 0.12	-0.96 ± 0.05	-0.96 ± 0.05
$\beta_{\rm d}$	1.49 ± 0.08	1.49 ± 0.12	1.49 ± 0.06	1.55 ± 0.06	1.52 ± 0.06	1.49 ± 0.05	1.44 ± 0.07
$T_{\rm d}$ (K)	19.37 ± 1.19	20.17 ± 1.52	19.20 ± 1.07	20.72 ± 1.03	20.10 ± 1.07	19.11 ± 0.95	18.54 ± 0.64
$\nu_{\rm AME}$ (GHz)	20.69 ± 1.91	22.84 ± 2.03	20.43 ± 1.78	21.50 ± 2.20	21.10 ± 1.73	20.39 ± 1.72	19.93 ± 1.99
$W_{\rm AME}$	0.56 ± 0.05	0.56 ± 0.04	0.56 ± 0.06	0.56 ± 0.04	0.57 ± 0.06	0.56 ± 0.06	0.56 ± 0.06
$I_{\rm AME}/S_{\rm total}^{\nu_{\rm AME}}$	0.46 ± 0.08	0.34 ± 0.05	0.48 ± 0.07	0.36 ± 0.06	0.49 ± 0.07	0.47 ± 0.07	0.48 ± 0.06
$I_{\rm AME}/S_{\rm total}^{28.4\,\rm GHz}$	0.44 ± 0.09	0.34 ± 0.05	0.45 ± 0.08	0.36 ± 0.06	0.48 ± 0.08	0.44 ± 0.09	0.47 ± 0.10
$I_{\rm AME}/S_{\rm ff}^{\nu_{\rm AME}}$	1.54 ± 0.45	1.48 ± 0.50	1.57 ± 0.47	1.54 ± 0.32	1.75 ± 0.58	1.60 ± 0.44	1.22 ± 0.26
$I_{\rm AME}/S_{\rm ff}^{28.4\,\rm GHz}$	1.35 ± 0.45	1.35 ± 0.49	1.36 ± 0.47	1.39 ± 0.30	1.50 ± 0.51	1.38 ± 0.45	1.02 ± 0.23
$\epsilon_{\rm AME}^{28.4\,\rm GHz}$ (μK MJy^{-1} sr)	11.62 ± 3.45	7.32 ± 2.07	12.18 ± 2.99	7.15 ± 2.27	10.76 ± 2.27	12.74 ± 2.86	14.15 ± 3.28

(and some others derived from them) are summarized in Table 5. If AME is expected to be the result of spinning dust (Draine & Lazarian 1998a, b), its emission will be correlated with the thermal emission from that same dust. This is explored in Figs D1 and D2, where the AME amplitude is compared with the dust opacity (τ_{353}) and radiance, respectively. The dust radiance is obtained as follows:

$$\mathfrak{R}_{\rm dust}(\tau_{353}, \beta_{\rm d}, T_{\rm d}) = \int_{-\infty}^{\infty} S_\nu^{\rm dust}(\tau_{353}, \beta_{\rm d}, T_{\rm d}){\rm d}\nu. \qquad (16)$$

The SRCC is a bit higher for $\mathfrak{R}_{\rm dust}$ than for τ_{353}, confirming the claim from Hensley et al. (2016) that $\mathfrak{R}_{\rm dust}$ is the best AME predictor (although is larger than 0.9 in both cases). These correlations were also found by PL14b, CA21, and P23. The uncertainties for these estimates have been computed as in Curran (2014), using 1000 different realizations. This is further explained in Appendix E. When studying these correlations, we selected only the pixels with $\mathrm{SNR_{AME}} > 2$, which account for $\simeq 47$ per cent of the sample. We chose the $\mathrm{SNR_{AME}}$ as a selection proxy to be sensitive to pixels high AME significance, instead to those with high flux density residuals between 20 and 60 GHz. The difference between the two estimates is important, as we are covering a large variety of regions. For example, the Cygnus region has large flux densities, but the AME fraction is low (below 25 per cent), as most of the emission is free–free. Nevertheless, these regions showing strong free–free emission are interesting to study the expected correlation between the dust temperature, $T_{\rm d}$, and star formation ratio, SFR, and therefore EM. The two do not appear correlated (*SRCC* = 0.013 ± 0.026) when studying all the pixels together due to the bad EM definition in most pixels of the plane. However, when using just those pixels with $\mathrm{SNR_{EM}} = \mathrm{EM}/\sigma(\mathrm{EM}) > 2$, the correlation between EM and $T_{\rm d}$ greatly increases to *SRCC* = 0.77 ± 0.03.

There are no big differences in SRCC values between the regions described in Section 4, but we find important differences (larger than 10σ) for the slopes from the corresponding fits. These are noticeable for the $A_{\rm AME}$ versus $\mathfrak{R}_{\rm dust}$ or τ_{353} relations (Fig. D2): the slope flattens (steepens) with increasing $\mathfrak{R}_{\rm dust}$ (τ_{353}) values (as for the Galactic Centre). This could have several causes: maybe there are different dust populations along the lines of sight that complicate the dust physics. In that case, our single MBB model would not completely solve that component. Or maybe the interstellar radiation field (ISRF) is too strong in this area, hence preventing the spinning grains from emitting AME as expected and partially destroying them instead (as happens in unresolved sources [Xie & Ho 2021] and photoionized gas [Dong & Draine 2011]). This could imply different correlations between the ISRF and the AME as we get close to the Galactic Centre, or generally between different regions. However, sources in low resolution (degree scales) analyses (such as those of PL14b,

Table 5. SRCC values for a series of selected variable pairs, taking into account only $\mathrm{SNR_{AME}} > 2$ pixels. Results are similar to those obtained placing the threshold at $\mathrm{SNR_{AME}} > 3$, while increasing the sample. N_pix accounts for the number of pixels considered for each region: we can see that it is anticorrelated with the SRCC uncertainties, as expected.

Variable 1	Variable 2	All pixels	Sector 1 ($\delta < -10^\circ$)	Sector 2 ($\delta > 13^\circ$)	Sector 3 ($\lvert l\rvert < 50^\circ$)	Sector 4 ($50^\circ \le l < 90^\circ$)	Sector 5 ($90^\circ \le l < 160^\circ$)	Sector 6 ($160^\circ \le l < 200^\circ$)
A_AME (Jy)	τ_{353}	0.90 ± 0.03	0.92 ± 0.02	0.89 ± 0.03	0.96 ± 0.02	0.94 ± 0.02	0.90 ± 0.03	0.84 ± 0.10
A_AME (Jy)	$\mathfrak{R}_\mathrm{dust}$ (Jy Hz)	0.95 ± 0.03	0.98 ± 0.02	0.96 ± 0.03	0.98 ± 0.02	0.98 ± 0.02	0.98 ± 0.03	0.90 ± 0.11
A_AME (Jy)	$S_\mathrm{TD,\,peak}$ (Jy)	0.96 ± 0.22	0.98 ± 0.12	0.97 ± 0.28	0.98 ± 0.12	0.98 ± 0.19	0.97 ± 0.32	0.90 ± 0.49
$A_\mathrm{AME}/\tau_{353}$ (Jy)	T_d (K)	0.76 ± 0.12	0.83 ± 0.14	0.76 ± 0.14	0.74 ± 0.14	0.73 ± 0.14	0.72 ± 0.16	0.52 ± 0.15
W_AME	$A_\mathrm{AME}/\tau_{353}$ (Jy)	0.44 ± 0.20	0.17 ± 0.09	0.51 ± 0.22	0.36 ± 0.21	0.68 ± 0.29	0.58 ± 0.27	0.05 ± 0.07
A_AME (Jy)	$\mathfrak{R}_\mathrm{AME}$ (Jy Hz)	0.97 ± 0.08	0.99 ± 0.13	0.96 ± 0.19	0.99 ± 0.12	0.97 ± 0.15	0.96 ± 0.21	0.93 ± 0.34
$S_\mathrm{TD,\,peak}$ (Jy)	EM ($\mathrm{pc\,cm^{-6}}$)	0.88 ± 0.27	0.93 ± 0.20	0.87 ± 0.36	0.97 ± 0.20	0.91 ± 0.27	0.91 ± 0.44	0.89 ± 0.60
A_AME (Jy)	EM ($\mathrm{pc\,cm^{-6}}$)	0.90 ± 0.14	0.94 ± 0.09	0.89 ± 0.16	0.98 ± 0.08	0.93 ± 0.10	0.90 ± 0.18	0.87 ± 0.27
$\mathfrak{R}_\mathrm{AME}$ (Jy Hz)	$\mathfrak{R}_\mathrm{dust}$ (Jy Hz)	0.92 ± 0.14	0.98 ± 0.05	0.93 ± 0.06	0.98 ± 0.04	0.94 ± 0.04	0.95 ± 0.07	0.84 ± 0.15
W_AME	T_d (K)	0.41 ± 0.17	0.25 ± 0.13	0.53 ± 0.20	0.27 ± 0.16	0.62 ± 0.24	0.65 ± 0.26	0.24 ± 0.15
ν_AME (GHz)	T_d (K)	0.63 ± 0.11	0.72 ± 0.15	0.64 ± 0.13	0.69 ± 0.13	0.66 ± 0.16	0.66 ± 0.15	0.52 ± 0.13
T_d (K)	EM ($\mathrm{pc\,cm^{-6}}$)	0.25 ± 0.03	0.49 ± 0.10	0.07 ± 0.03	0.43 ± 0.08	0.00 ± 0.05	0.07 ± 0.03	0.09 ± 0.06
A_AME (Jy)	T_d (K)	0.29 ± 0.02	0.54 ± 0.06	0.13 ± 0.02	0.40 ± 0.06	-0.15 ± 0.04	0.08 ± 0.03	0.04 ± 0.06
$A_\mathrm{AME}/\tau_{353}$ (Jy)	EM ($\mathrm{pc\,cm^{-6}}$)	0.37 ± 0.07	0.58 ± 0.15	0.29 ± 0.06	0.64 ± 0.12	0.29 ± 0.08	0.31 ± 0.08	0.18 ± 0.10
ν_AME (GHz)	EM ($\mathrm{pc\,cm^{-6}}$)	0.42 ± 0.08	0.69 ± 0.69	0.32 ± 0.32	0.61 ± 0.61	0.35 ± 0.34	0.30 ± 0.29	0.28 ± 0.27
	N_pix	2437	257	1985	417	513	1142	317

CA21, P23, and this study) appear too faint owing to dilution in the beam: the A_AME versus $\mathfrak{R}_\mathrm{dust}$ relation seems to bend at $\mathfrak{R}_\mathrm{dust} = 10^9$ Jy Hz. Observations at higher resolution of compact AME sources are needed to fully sample this behaviour, as stronger ISRFs or $\mathfrak{R}_\mathrm{dust}$ values are required.

We report another correlation between the dust temperature, T_d, and the AME peak frequency, ν_AME, as showed in Fig. D3. A similar dependence is recovered between ν_AME and the ISRF strength proxy, G_0, obtained as in Mathis, Mezger & Panagia (1983):

$$G_0 \equiv \left(\frac{T_\mathrm{d}}{T_0}\right)^{4+\beta_\mathrm{d}} \tag{17}$$

with $T_0 = 17.5$ K. We see that β_d has little impact on the behaviour of G_0, so T_d dominates it: in fact, the correlations of G_0 and T_d with other components are often very similar. This is the case for the correlations between T_d and G_0 with ν_AME, which return identical results (0.63 ± 0.11). This result is consistent with those obtained by PL14b and CA21 (0.65 ± 0.15 and 0.60 ± 0.07, respectively), while P23 founds a correlation only for its semi-significant AME sample (0.60 ± 0.15). Andersen et al. (2023) found a positive correlation between ν_AME and β_d (SRCC = 0.85) instead of T_d. However, in that case T_d is fixed to the results obtained with the NPIPE pipeline on *Planck* DR4 (Planck Collaboration 2020). Both cases probably indicate the same relation between the location of spinning and thermal dust emission peaks in the frequency range, but in one case the correlation is found when comparing to T_d and in the other when comparing with β_d. Neither did we find any correlations between ν_AME and β_d (0.00 ± 0.04) nor between β_d and T_d (0.13 ± 0.04). The full set of correlations between the parameters studied can be seen in Table D1, the most interesting feature being the lack of correlations between W_AME and all the other parameters.

Other differences between this study, CA21 and P23 are:

(i) the EM versus ν_AME correlation, which is 0.42 ± 0.08 in this study, 0.80 ± 0.03 in CA21 (>4σ away; with no synchrotron present) and negative or absent in P23 (depending on the exact sample);

(ii) the correlation between the AME emissivity, defined as $A_\mathrm{AME}/\tau_{353}$,[12] and W_AME, which is less important here (∼0.44 ± 0.20) than in P23 (∼0.60 ± 0.15);

(iii) the absence of correlation between EM and T_d in this study, 0.25 ± 0.03, partly compatible with P23 (depending on the exact sample), while CA21 finds a higher degree of correlation (0.65 ± 0.07), probably due to EM being best constrained.

In any case, it is difficult to compare the free–free related correlations between the previous two studies and this one, as no synchrotron component was used in CA21. P23 introduced it only for a few sources, mostly supernova remnants, where the presence of synchrotron was evident.

On the other hand, this study, CA21 and P23 find similar results for the correlation between the AME emissivity and T_d (0.76 ± 0.12, 0.82 ± 0.06, and ≃0.68 ± 0.08, respectively; see Figs D4 and D5). PL14b found a lower value, 0.63 ± 0.07, which is still consistent within 1σ with our result. The linear fits describing both this relation and the T_d versus ν_AME one are consistent across the regions considered. However, when calculating the AME emissivity using a different dust tracer, as could be the dust radiance ($A_\mathrm{AME}/\mathcal{R}_\mathrm{dust}$) or the previously presented intensity at 100 μm ($\epsilon_\mathrm{AME}^{28.4\,\mathrm{GHz}}$), this correlation is absent (−0.43 ± 0.09 and −0.42 ± 0.07). This issue is further discussed on Section 5.2.1.

Finally, we find significant correlations between the amplitudes of synchrotron ($A_{1\,\mathrm{GHz}}$), free–free (EM), AME (A_AME), and thermal dust (τ_{353}). Studying a region so heavily populated as the Galactic plane, we detect very large variations for the column density of the pixels. A pixel with many environments along its line of sight is more likely to have large amplitudes for all components. CA21 and P23 did not fully recover this, as they were not so sensitive to the different line-of-sight densities. For example, the EM versus A_AME relation was not studied in the former, while bringing coherent results between

---

[12] This emissivity definition is analogous to that in Section 4.2, as we still compare AME to thermal dust emission. We use now this definition to be consistent with the analyses of CA21 and P23, both using QUIJOTE-MFI data too.

selections in the latter (0.59 ± 0.05/0.65 ± 0.11), depending on the sample. On the other hand, we got a higher correlation value of 0.90 ± 0.14.

5 DISCUSSION

5.1 Impact of QUIJOTE-MFI on the characterization of the Galactic plane

In order to properly assess the increased capability of recovering the AME properties provided by the addition of QUIJOTE-MFI data, we applied the same methodology, but now without QUIJOTE-MFI (the rest of the survey set from Table 1 remains the same). For clarity, we named these two cases as 'FULL' when the QUIJOTE-MFI points are taken into account, and 'noMFI' otherwise. The results can be seen in Fig. 10, where we show how $\mathrm{SNR}_{\mathrm{AME}}$ changes. $\mathrm{SNR}_{\mathrm{AME}}$ is higher for the FULL case, with great improvement towards the areas where AME is not detected at all in the noMFI case (farther away from the plane). In the FULL case, these regions have marginal detections, predominantly with $\mathrm{SNR}_{\mathrm{AME}}$ between 2 and 3.

Focusing on the parameters, we can see in Figs 10 and 11 how α_{syn} changes towards flatter values in the noMFI case, especially close to the Fan region ($l \sim 110^\circ$). In Fig. 10, we also show that I_{AME} values are lower in the noMFI case, free–free signal thus increasing. For example, the same SED showed in Fig. 3, when computed in the noMFI case, returns an AME flux density fraction at 28.4 GHz lower than half its previous value (from 53 per cent to 21 per cent). That difference is mostly accounted for by free–free. The clear anticorrelation pattern between *EM* and A_{AME} present on Fig. 4 also worsens in the noMFI case. The dust parameters do not change significantly, as expected: data between 10 and 20 GHz should not constrain a component that rises beyond 100 GHz.

There is an excess for the total flux density from the fits at 11.2 GHz in the noMFI case, when compared with the obtained in the FULL one. This difference is higher than 3σ [σ being the uncertainty from equation (11) at 11.2 GHz in the FULL case] for most of the pixels. This is particularly evident when focusing on those pixels with $\mathrm{SNR}_{\mathrm{AME}} > 2$, which are the ones primarily studied here (Fig. 12). Plotting this difference against $\mathrm{SNR}_{\mathrm{AME}}$ in the FULL case, we see a clear trend. The excess is more important for those pixels with higher AME significance. This is as expected: a pixel described by synchrotron or free–free, or the sum of both, will have a more similar behaviour between the low (1–10 GHz) and medium (10–100 GHz) frequency domains, compared to one with a rising AME component. A similar result can be seen in Fig. 13, where it is clear that the pixels with the highest AME significances show the greatest free–free excesses in the noMFI case. On the other hand, the synchrotron amplitude ($I_{1\,\mathrm{GHz}}$) estimates are also higher in the noMFI case, but those excesses are similar between pixels with high and low AME significances.

This analysis illustrates the importance of having reliable data in the 10–20 GHz region. These data are required to avoid overestimating the free–free and/or synchrotron component (due to α_{syn} flattening), as will happen when the flux density is higher at those frequencies. The increasing flux density towards WMAP and LFI bands should then be accounted for by the AME, thus increasing the expected importance of this component within the diffuse emission. PL16 partly solved this issue primarily by fixing the synchrotron spectral index, thus preventing the low frequency foregrounds from accounting for that difference.

5.2 Correlations between the AME amplitude map and the frequency maps between 0.408 GHz and 8 micron

We compared our A_{AME} map from Fig. 5 with all frequency maps present in Table 1. Besides, we introduced the maps from the COBE-DIRBE (Hauser et al. 1998) with wavelengths shorter than 100 μm that were not used in the SED fitting, down to 12 μm. Data at 8 μm from the Spitzer (Fazio et al. 2004; Werner et al. 2004) satellite was also introduced. For COBE-DIRBE, we used the released version with zodiacal light subtracted. We also considered Infrared Astronomical Satellite maps [IRAS; Neugebauer et al. (1984), Wheelock et al. (1994)], but the zodiacal light emission was still present in those maps, even when using IRIS[13] (Miville-Deschênes & Lagache 2005) data. For this reason, we used COBE-DIRBE data, in which a small residual from the zodiacal light is still visible, especially at 12 and 25 µm. IRAS data are also available through the LAMBDA, while for Spitzer we used the 8 µm GLIMPSE (Churchwell et al. 2009) data available in the Centre d'Analyse de Données Etendues (CADE, Paradis et al. 2012) webpage[14] and already in HEALPIX format. This last map does not cover the full Galactic plane: we have avoided pixels closer to 1° to the non-observed part of the map to prevent issues arising from the 1° smoothing and downgrading to HEALPIX $N_{\mathrm{side}} = 64$. The smaller number of available pixels imply greater uncertainty estimates when computing the correlations between this Spitzer map and the parameter maps. This is especially important for $90^\circ < l < 160^\circ$ and the anticentre regions. In Table 6 we show the correlations between the maps from COBE-DIRBE and Spitzer when compared to the A_{AME} parameter map obtained in this study. Fig. 14 shows the correlation values with A_{AME} for all the frequency maps listed in Table 1.

The correlation between the AME amplitude, A_{AME}, and the maps is good from the mid- to the far-infrared (8–100 µm). An example for these correlations is shown in Fig. 15, for the Spitzer 8 µm map. This case is particularly remarkable, as all the data come from just two positions of the sky: the first covers the Galactic Centre, while the second focuses on those pixels with $l > 30^\circ$. We see that the behaviour is different between the two regions, although consistent within the uncertainties. As the region covering the Galactic Centre probably hosts more heterogeneous environments along its lines of sight, the latter is better for making comparisons between surveys. SRCC increases from 0.904 ± 0.028, when all pixels are studied together, to 0.979 ± 0.035, when studying just the $l > 30^\circ$ region. On the other hand, we find that the correlation factor decreases for the DIRBE 60 and 25 µm bands when the $l > 30^\circ$ limit is applied, down to 0.878 ± 0.025 and 0.861 ± 0.027, respectively. The values for 60–25 μm are 2.3–2.6σ lower than those recovered for the Spitzer 8 µm band, and lower than $\sim 2\sigma$ than those from e.g. *Planck-HFI* 857 GHz or COBE-DIRBE 240 μm. We note that this high level of correlation between the dust and the AME in the full Galactic plane was obtained introducing minimal priors.

5.2.1 *Implications on preferred AME carriers from correlations between AME and far-infrared surveys*

Since the first works proposing theoretical models to explain the AME as spinning radiation from dust grains (Draine & Lazarian 1998b), PAHs have been the preferred proposed carriers for this emission. The thermal emission from dust grains with the small size

---

[13] Improved Reprocessing of the IRAS Survey.

[14] http://cade.irap.omp.eu/dokuwiki/doku.php

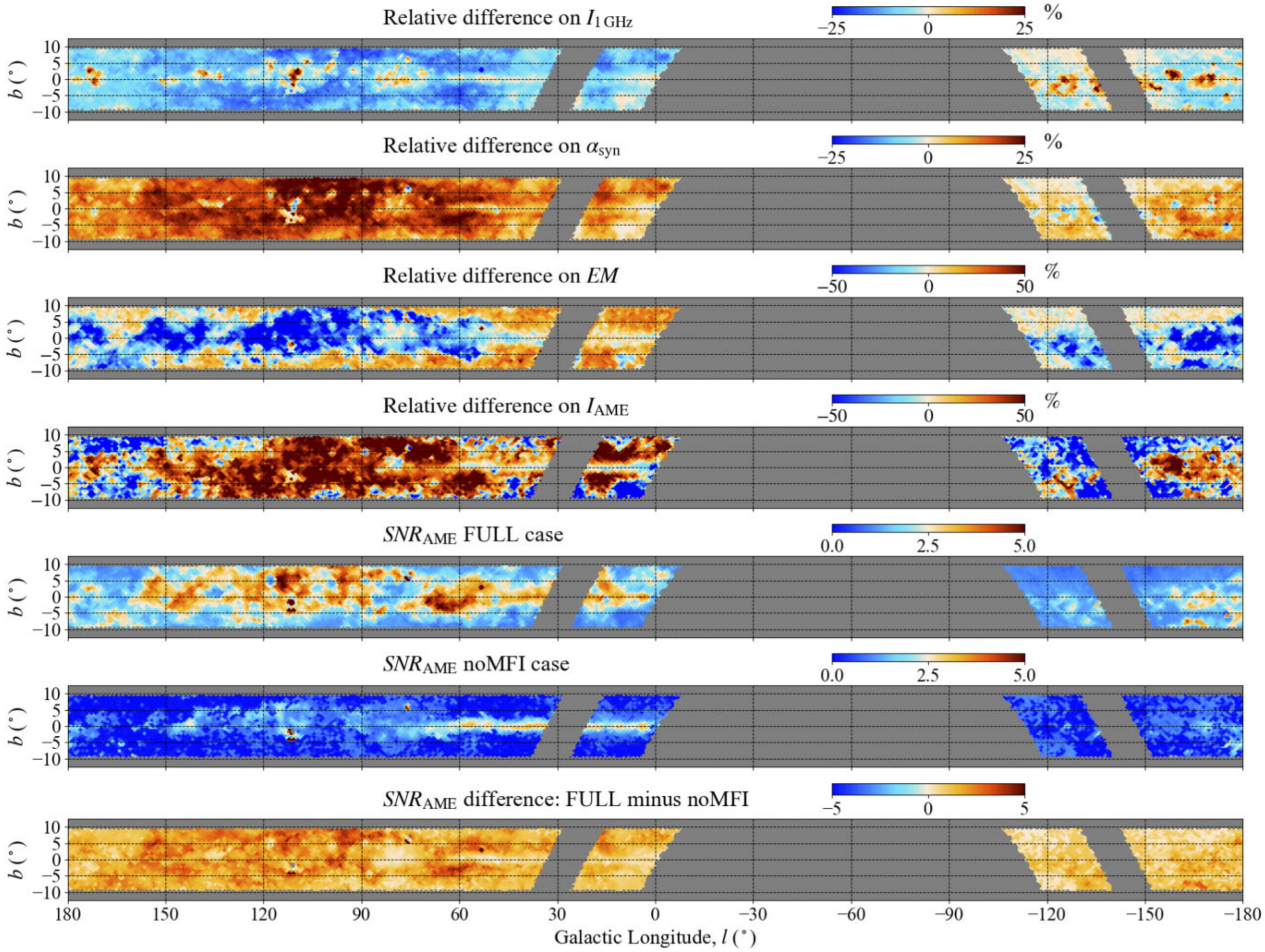

Figure 10. Top two: relative differences for the two synchrotron parameters when using, or not using, the MFI points to build the SEDs. Differences are calculated as the estimate for the FULL case minus the one from noMFI case, divided by the first one. Next two: relative differences for the parameters driving free–free and AME intensities. We see that AME is more important when QUIJOTE-MFI data is taken into account (FULL scenario), while free–free gains importance when it is not (noMFI scenario). Bottom three: differences in SNR$_{\mathrm{AME}}$ when the QUIJOTE points are added to the survey set.

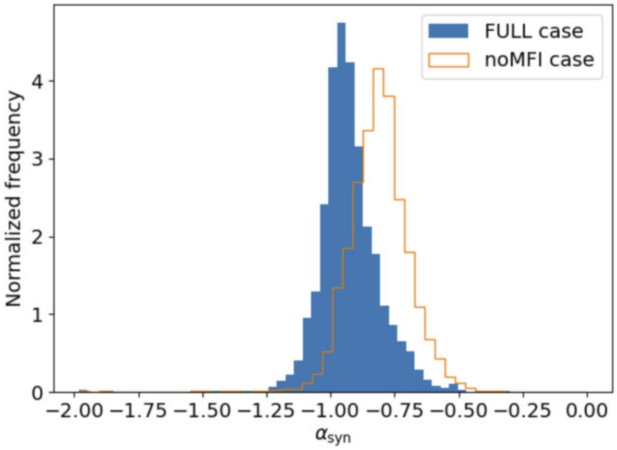

Figure 11. Distribution for α_{syn}, both with and without MFI points. We see how, in the latter case, the results are displaced towards higher values: from $\alpha_{\mathrm{syn}} = -0.95^{+0.15}_{-0.09}$ to $\alpha_{\mathrm{syn}} = -0.84^{+0.13}_{-0.09}$ (both are consistent within 1σ, though).

of PAHs ($a_0 \sim 0.64$ nm) show up in the mid-to-near infrared region of the ISM spectrum, while their emission due to an hypothetical spinning mechanism would lie in the microwave, thus possibly accounting for AME. PAHs spectra present several emission lines and features (both broad and narrow) between 1 and 12 μm (see e.g. fig. 2 of Compiègne et al. 2011): we are mostly interested on the 7.7 μm emission line, as it is within the Spitzer 8 μm band. This allows us to use this band as a PAH tracer.[15] Between 30 and 50 μm wavelengths generic small amorphous carbon grains (VSGs) are the main emitting molecules: for larger wavelengths, emission from big dust grains (BGs, either amorphous carbon or amorphous silicates, with $a_0 \in (1, 100)$ nm) dominates. Finally, it is worth noting that the average Galactic PAH emission per H atom and normalized by G_0 has very little sensitivity to G_0. This is because the almost linear dependency of PAH emissivity per H atom with G_0 is largely cancelled out after normalizing by G_0 [see Fig. 7 of Compiègne et al.

---

[15] Hensley, Murray & Dodici (2022) showed that a lower correlation between the PAH 11.3 μm line – and thus COBE-DIRBE 12 μm band – and AME could be expected even if PAHs are responsible for AME.

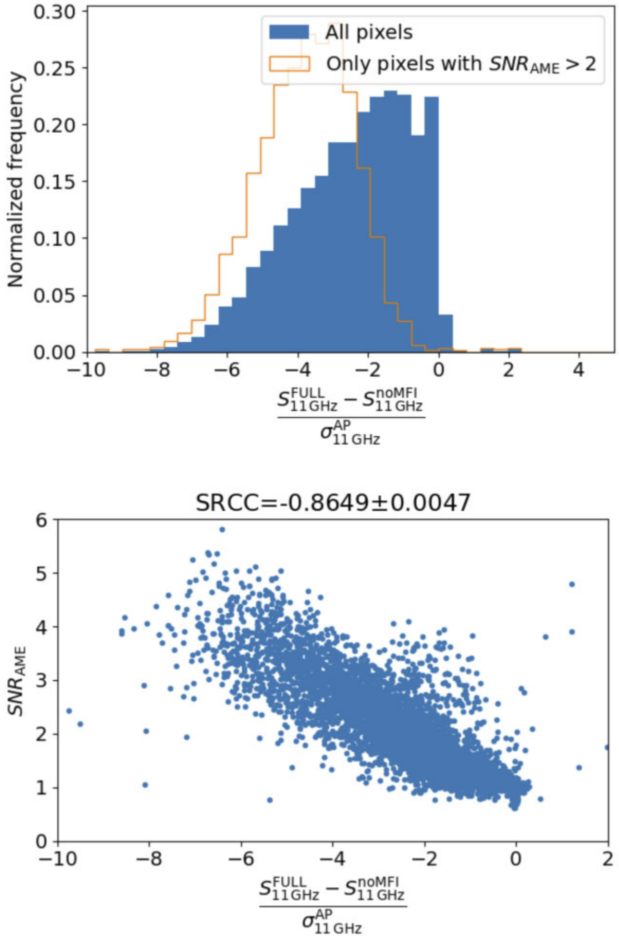

Figure 12. Top: histograms of the difference in the flux density predicted by the fitted model at 11.2 GHz between the FULL and noMFI cases, over the uncertainty obtained for the SED in the FULL scenario. We see how most of the pixels (especially when focusing on those with $\mathrm{SNR}_{\rm AME} > 2$) have non-negligible differences between the two cases. Bottom: The same difference, but now plotted versus $\mathrm{SNR}_{\rm AME}$ from FULL case. There is a clear trend, the flux density deficit being more important for those pixels with higher AME significance.

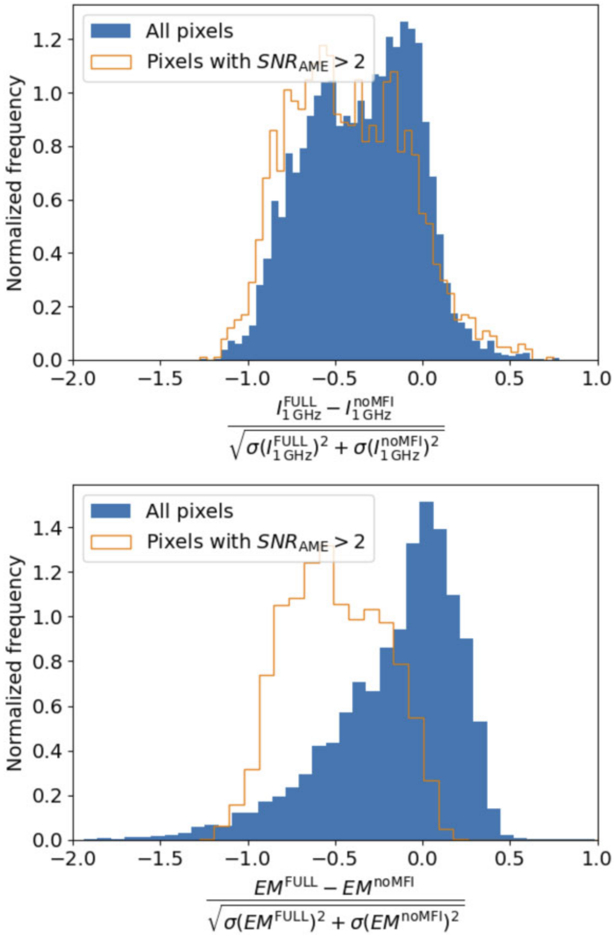

Figure 13. Top: Comparison between FULL and noMFI cases for $I_{1\,\rm GHz}$. We have plotted the difference between the two estimates over their quadratic uncertainty. Bottom: Equivalent histogram for *EM*. The difference peaks around zero when studying all the pixels, but it is clearly displaced towards lower values (higher free–free estimates for the noMFI case) when focusing on pixels with high AME significance.

(2011), where G_0 is noted as U]. MBB emission from large grains, on the other hand, shows a more complicated dependence with G_0.

Therefore, the higher SRCC between $A_{\rm AME}$ and 8 μm compared to $A_{\rm AME}$ and 24–60 μm implies a marginal preference for spinning dust from PAHs (or nanocarbons) over other VSGs (or nanosilicates) as the main carrier. However, the correlation between the AME map and the 8 μm one is comparable to those between the AME map and those tracing thermal dust emission from BGs (e.g. COBE-DIRBE 100 μm). Besides, we explained how PAH emission (and thus, its 7.7 μm band) is not correlated with G_0, while the emission from BGs is, as well as the AME emissivity when computed as $A_{\rm AME}/\tau_{353}$ (Section 4.3). This, together with the important correlation between the AME and the BGs emission bands, could be pointing to BGs being the main AME carrier instead of PAHs or VSGs (Chuss et al. 2022). This apparent non-PAH origin of AME, which contradicts many of the first works focused on AME as spinning dust emission, has been also proposed in recent studies: both Hensley et al. (2015) and Murphy et al. (2018) found AME estimates too large in extragalactic regions to be solely explained by PAHs, while Hensley et al. (2016) and Hensley & Draine (2017) showed that other carriers – such as silicates, as later demonstrated by Ysard et al. (2022) – could account for the entirety of AME with no PAH contribution at all.

However, even the correlation between the AME emissivity and G_0 is unclear. Although $A_{\rm AME}/\tau_{353}$ and G_0 show a strong correlation, when using other dust tracers to build the AME emissivity the correlation disappears, as introduced in Section 4.3. For example, when building the AME emissivity as in Section 4.2, i.e. using the ratio between the AME intensity at 28.4 GHz (in temperature units) and the dust intensity at 100 μm, $\epsilon^{28.4\,\rm GHz}_{\rm AME}$, we find that it is slightly anticorrelated with G_0, with $SRCC = -0.42 \pm 0.07$. We obtain the same result when using the total dust radiance, as defined in Section 4.3, as the dust tracer: $A_{\rm AME}/\mathcal{R}_{\rm dust}$ versus G_0 return $SRCC = -0.43 \pm 0.09$. These differences between the correlations with G_0 when using different dust tracers were already presented in CA21 (see H and L panels on their Fig. 6).

These apparently contradictory findings contribute to the still open and unclear situation on AME carriers within the community (e.g. Dickinson et al. 2018). Considering them together with the low significant differences between the correlations when comparing $A_{\rm AME}$ with the different frequency maps (most are consistent within 1–2σ), it is difficult to provide a strong claim as to what is the preferred AME carrier. The only differences greater than 3σ on

Table 6. SRCC values between the AME amplitude (A_{AME}) and several surveys mapping the far-infrared sky emission, only for those pixels with $\mathrm{SNR}_{\mathrm{AME}} > 2$. Every band has a high correlation degree with the A_{AME} map.

Map	All pixels	Sector 1 ($\delta < -10^\circ$)	Sector 2 ($\delta > 13^\circ$)	Sector 3 ($\lvert l \rvert < 50^\circ$)	Sector 4 ($50^\circ \le l < 90^\circ$)	Sector 5 ($90^\circ \le l < 160^\circ$)	Sector 6 ($160^\circ \le l < 200^\circ$)
DIRBE 240 µm	0.96 ± 0.03	0.98 ± 0.02	0.96 ± 0.03	0.98 ± 0.02	0.97 ± 0.02	0.96 ± 0.04	0.88 ± 0.12
DIRBE 140 µm	0.95 ± 0.03	0.98 ± 0.02	0.96 ± 0.03	0.98 ± 0.02	0.98 ± 0.02	0.98 ± 0.03	0.91 ± 0.12
DIRBE 100 µm	0.93 ± 0.03	0.98 ± 0.02	0.93 ± 0.03	0.98 ± 0.02	0.98 ± 0.02	0.96 ± 0.04	0.90 ± 0.13
DIRBE 60 µm	0.89 ± 0.02	0.97 ± 0.02	0.88 ± 0.03	0.97 ± 0.02	0.97 ± 0.02	0.92 ± 0.03	0.85 ± 0.11
DIRBE 25 µm	0.88 ± 0.02	0.97 ± 0.02	0.87 ± 0.03	0.97 ± 0.02	0.96 ± 0.02	0.94 ± 0.04	0.32 ± 0.06
DIRBE 12 µm	0.92 ± 0.03	0.97 ± 0.02	0.92 ± 0.03	0.98 ± 0.02	0.97 ± 0.02	0.93 ± 0.03	0.52 ± 0.07
Spitzer 8 µm	0.90 ± 0.00	0.93 ± 0.04	0.96 ± 0.05	0.86 ± 0.04	0.97 ± 0.14	0.49 ± 0.21	—

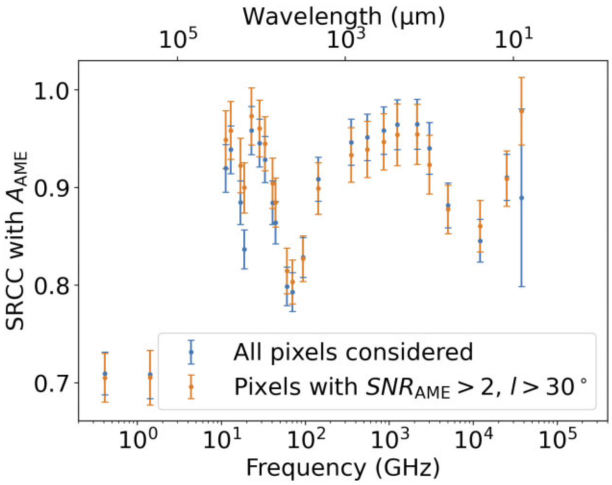

Figure 14. SRCC values between the various frequency maps and the A_{AME} map: we see that the correlation is high for most of the bands. We used only those pixels with high AME significance ($\mathrm{SNR}_{\mathrm{AME}} > 2$) for this figure. We are highlighting the difference between studying all pixels and only those with $l > 30^\circ$. This difference is especially important for Spitzer 8 µm case, as pointed out in Fig. 15.

the A_{AME} and frequency maps correlations are the ones comparing COBE-DIRBE 25 and 60 μm bands, which would trace VSGs, with respect to 240 and 140 μm bands, tracing BGs. Even in this case, this significance level is only reached when applying the $l > 30^\circ$ selection. PL14b and P23 also found no evident preference for any far-infrared band. On the other hand, CA21 found that the SRCC was as low as 0.4–0.7 for the 100–25 µm bands, and then increased for the mid-infrared bands (12 µm and AKARI 9 µm[16] maps, Bell et al. 2019). This is similar to our results, but we find much less pronounced differences, partly owing to the wider variety of regions studied along the Galactic plane, instead of a single and isolated one, such as λOrionis. But the main difference between CA21 and this study is the absence of correlation between A_{AME} and the frequency bands below 100 GHz in the former. This is due to the fact that in that case for the frequency maps where the AME is brighter (between 20 and 30 GHz) there is a lot of free–free emission in the inner hydrogen shell. This is still much brighter than the AME in the ring that surrounds the region and that is smearing the correlation. Finally, we should mention that Vidal et al. (2020) found the highest correlation between AME and the FIR bands at 70 µm when studying LDN 1780 on arcmin scales. This was the lowest correlated band in the CA21 analysis (60 µm in that case, which is also the second least correlated band in our analysis, after 25 μm). Nevertheless, this was attributed to LDN 1780 not being in local thermal equilibrium, so the comparison is difficult. The difference between the two cases could be due to that issue instead of the different angular scales, which was shown in Arce-Tord et al. (2020).

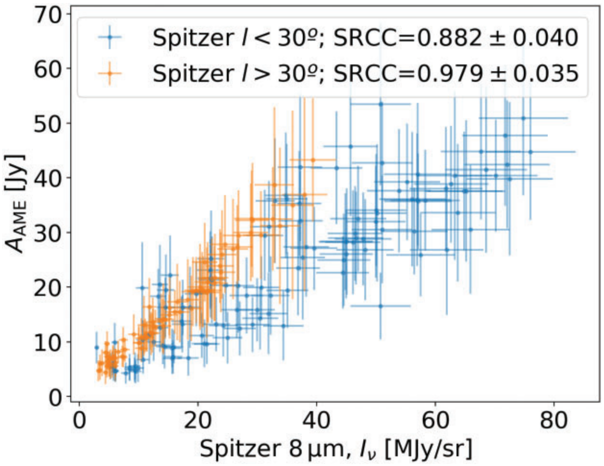

Figure 15. Correlations between the AME amplitude and the 8 µm Spitzer map. Most of the data come from two regions: the Galactic Centre and $l > 30^\circ$. It is clear that the two areas behave differently.

Because of the strong correlations between the AME map and almost every emission map (SRCC is higher than 0.8 for all the surveys between 10 GHz and 8 μm), we believe that the full Galactic plane is too heterogeneous a sample to build AME relations with different tracers. Many authors have proposed in the past that AME is extremely sensitive to the local properties within its environment (e.g. Hensley et al. 2022). Studying the Galactic plane as a whole implies the mixing of really different environments, not only within the lines of sight but also when binning the different longitude regions. This is extremely important in this kind of study, but not as much when focusing on the high latitude sky (e.g. Harper et al. 2022) or resolved regions (CA21).

5.3 Comparison with PL16

We next compare our results with those obtained using the COMMANDER code in PL16. We chose to compare our results with the COMMANDER ones instead of those from the previously mentioned studies (Planck Collaboration 2014a, 2015a) because the methodology and area to be studied are more similar. For example, a break in the dust index at 353 GHz was introduced in those two works and

---

[16] Which was used instead of the Spitzer 8 µm band.

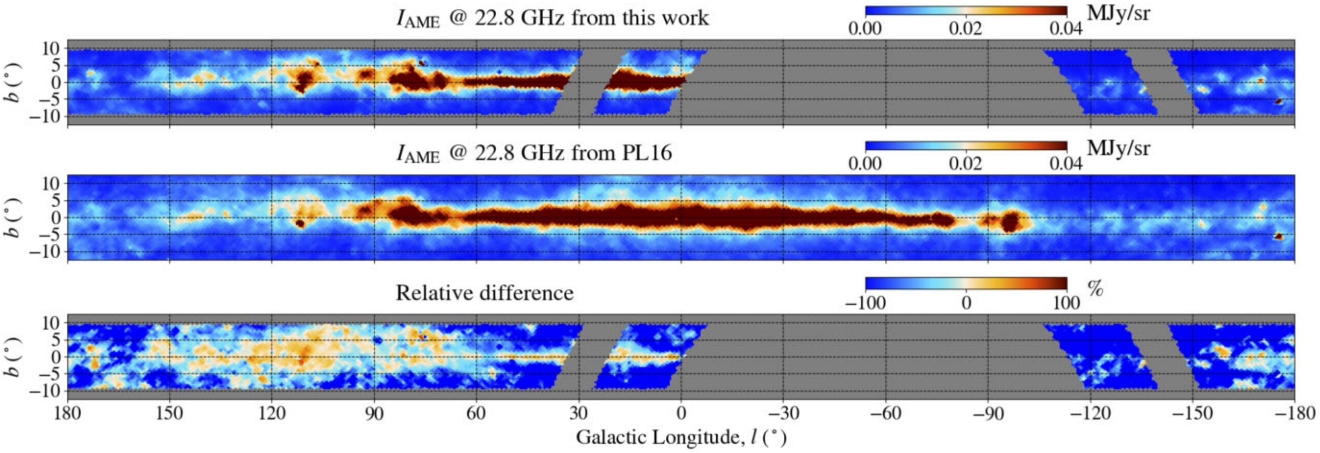

Figure 16. Comparison maps between our study and PL16 for the AME. The first two are the AME intensity at 22.8 GHz (from this study and PL16, respectively): we chose to plot the difference at a fixed, representative frequency owing to the differences between the two methodologies used to model the AME. The third one is the relative difference between the two, computed as the estimate from this study minus the one from PL16, divided by the former.

was neither used nor required in our low-resolution analysis. There are crucial differences, though, between this study and that of PL16, the most important one being the addition of information from the low-frequency (below 20 GHz) surveys, especially from QUIJOTE-MFI, which were not available for PL16. The methodologies also differ between the two studies: whereas we are using a single log-normal distribution to fit for the AME, PL16 used two components, one representing cold neutral medium and the other representing warm neutral medium (WNM). The approach behind these two distributions is not phenomenological, as in our case, but was instead driven by the physics of the dust. For that purpose, they used SPDUST software[17] to model the spinning dust emission in the two scenarios. Regarding the synchrotron fitting, PL16 used a spatially constant $\alpha_{\rm syn}$ derived from a model assuming a certain propagation of cosmic ray scenario through the Galactic magnetic field (GALPROP ; Orlando & Strong 2013; Planck Collaboration 2016b). $\alpha_{\rm syn}$ varies with frequency in this model, being flatter (higher than −1) at lower frequencies and then steeper (and almost constant to −1.1) at higher (above 1 GHz) frequencies. On the other hand, we assume a spatially dependent (as suggested by the analysis of the QUIJOTE-MFI maps in the Wide Survey data release, e.g. de la Hoz et al. 2023; Rubiño-Martín et al. 2023), but frequency invariant, $\alpha_{\rm syn}$ value. Besides, PL16 applied a Gaussian prior to the dust parameters $\beta_{\rm d}$ and $T_{\rm d}$, while we use a flat prior (from Table 2). The Gaussian $\beta_{\rm d}$ prior was particularly important, with median and standard deviation equal to 1.55 and 0.1, respectively; this prior is clearly imprinted in the reconstructed dust spectrum when studying the pixel-value distribution. Finally, the full intensity signal is fitted in PL16, while in our study a background level is subtracted.

Our recovered $\alpha_{\rm syn}$ median value is -0.94 ± 0.10, which is flatter than the usual −1.1 value used to model the synchrotron. This is due to the fact that Haslam et al. (1982) and Berkhuijsen (1972) data points have the lowest calibration uncertainties among all our low frequency data, so the two drive the fit at those frequencies. We mentioned previously that the GALPROP model used by PL16 expects a flatter synchrotron component at those frequencies below 1 GHz. Therefore, our synchrotron estimates at higher frequencies are larger than those from PL16. This causes free–free estimates to be lower, due to the important degeneracy between the two components.

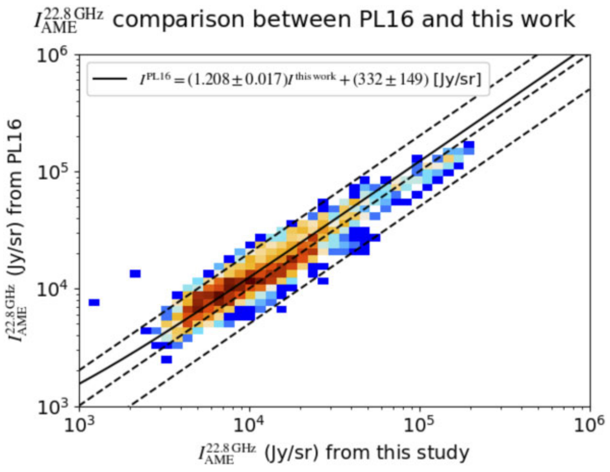

Figure 17. Correlation plot for the AME intensity estimates at 22.8 GHz from this work and PL16. Only those pixels with $\mathrm{SNR}_{\rm AME} > 2$ in this study are plotted. Dashed lines mark the 0.5, 1, and 2 comparison levels. The best linear fit is also provided and shown as a solid line. The slope is slightly higher than unity due to the excess of higher $I_{\rm AME}$ values from PL16 at low values ($0.5\text{–}1.0 \times 10^4$ Jy sr^{-1}).

However, when comparing the AME intensity estimates from both studies, we find that differences are small for those pixels detected with good SNR (Fig. 16). Our estimates are lower as we get farther away from the plane. The map showing the relative difference resembles the map tracking the AME fraction in both studies. This suggests that the AME amplitude reconstruction is stable in those pixels where the component is important. In Fig. 17, we show the correlation plot between the two $I_{\rm AME}$ estimates from both studies. A slight excess from PL16 is visible for those pixels with low $I_{\rm AME}$ (probably those pixels farther from the plane).

Finally, the addition of the three frequency points from COBE-DIRBE, together with the previously mentioned differences with PL16 on the priors, produces a shift in the dust parameters values. We find slightly lower (higher) values for $\beta_{\rm d}$ ($T_{\rm d}$), since the two parameters are known to be anticorrelated: both kinds of behaviours are shown in Fig. 18. We can also see in Fig. 8 how the variation of $T_{\rm d}$

---

[17] Which shows $W_{\rm AME}$ values slightly incompatible with those found in this study, as discussed in Section 4.1.

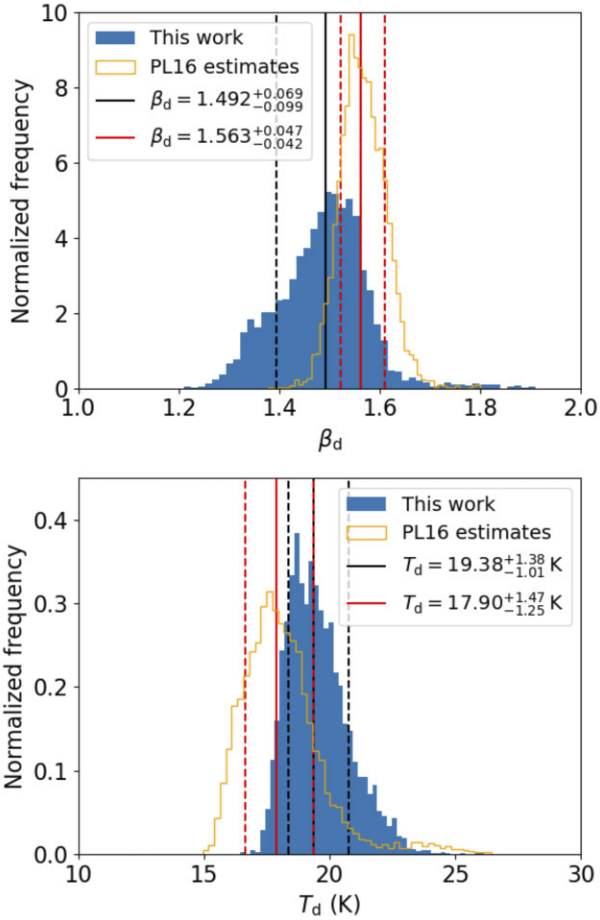

Figure 18. Comparison of the dust parameter distribution between PL16 and this study. We see that β_d (top) is displaced towards lower values in comparison with PL16, while the behaviour of T_d (bottom) is the opposite. In the first case, PL16 distribution seems to follow the Gaussian prior, $N(1.55 \pm 0.1)$ from Table 4 in PL16, while for the second the results are far from their prior centre, $N(23 \pm 3)$ K.

with latitude is similar, apart from a certain offset, for both this study and PL16, while β_d from the latter remains fairly constant because of the previously mentioned prior. These differences between the two methodologies (in particular in the applied priors) make a quantitative comparison difficult.

6 CONCLUSIONS

We have presented a set of 10 maps for the parameters describing the various diffuse microwave emission components (synchrotron, free–free, AME, thermal dust, and CMB anisotropies) along the Galactic plane ($|b| < 10^\circ$) at 1 degree angular scales. For this purpose, we introduced new data from the QUIJOTE-MFI Wide Survey between 10 and 20 GHz and used a fitting methodology assuming minimal priors, thus removing any possible biases. This is one of the first works to show spatial variations in the synchrotron index along the Galactic plane in intensity using WMAP and *Planck* data. Spatial variations for the AME spectral parameters are also hinted, but with reduced statistical significance. However, the obtained median values disagree with those from theoretical models, pointing to lower (higher) $\nu_{\rm AME}$ ($W_{\rm AME}$) values than first expected. We have also shown how having reliable data between 10 and 20 GHz is mandatory to avoid overestimating synchrotron against free–free and AME.

Future studies should focus on improving results through the addition of more frequency data. This is especially important at lower frequencies, where the foregrounds are heavily degenerate. Introducing C-BASS data at 5 GHz (Irfan et al. 2015; Jones et al. 2018) will further improve the separation between synchrotron and free–free, and consequently AME. Repeating the analysis in polarization would also be interesting, as the degeneracies are not expected to be as important (free–free and AME are negligibly polarized compared to synchrotron and thermal dust). However, additional work would be required to properly correct for possible issues of depolarization and Faraday rotation. Low-frequency data in polarization are also much scarcer than intensity data. Finally, repeating this analysis at higher angular resolutions, aiming for arcminute scales, would be interesting. Previous studies (Arce-Tord et al. 2020) have hinted that the AME relation with thermal dust (and therefore mid- to far-infrared surveys) could change with higher angular resolution observations. However, studying the entire Galactic plane at high angular resolution is probably unrealistic, so the focus should go into smaller, resolved and isolated regions such as λOrionis (CA21).

ACKNOWLEDGEMENTS

We thank the staff of the Teide Observatory for invaluable assistance in the commissioning and operation of QUIJOTE. The *QUIJOTE* experiment is being developed by the Instituto de Astrofisica de Canarias (IAC), the Instituto de Fisica de Cantabria (IFCA), and the Universities of Cantabria, Manchester and Cambridge. Partial financial support was provided by the Spanish Ministry of Science and Innovation under the projects AYA2007-68058-C03-01, AYA2007-68058-C03-02, AYA2010-21766-C03-01, AYA2010-21766-C03-02, AYA2014-60438-P, ESP2015-70646-C2-1-R, AYA2017-84185-P, ESP2017-83921-C2-1-R, PID2019-110610RB-C21, PID2020-120514GB-I00, IACA13-3E-2336, IACA15-BE-3707, EQC2018-004918-P, the Severo Ochoa Programs SEV-2015-0548 and CEX2019-000920-S, the Maria de Maeztu Program MDM-2017-0765 and by the Consolider-Ingenio project CSD2010-00064 (EPI: Exploring the Physics of Inflation). We acknowledge support from the ACIISI, Consejeria de Economia, Conocimiento y Empleo del Gobierno de Canarias and the European Regional Development Fund (ERDF) under grant with reference ProID2020010108. This project has received funding from the European Union's Horizon 2020 research and innovation program under grant agreement number 687312 (RADIOFOREGROUNDS).

We thank the anonymous referee whose comments helped to improve this work. We also thank Bruce Draine, Brandon Hensley, and Enrique Fernández Cancio for their useful comments. MFT acknowledges support from the Agencia Estatal de Investigación (AEI) of the Ministerio de Ciencia, Innovación y Universidades (MCIU) and the European Social Fund (ESF) under grant with reference PRE-C-2018-0067. SEH acknowledges support from the STFC Consolidated Grant (ST/P000649/1). FP acknowledges support from the Spanish State Research Agency (AEI) under grant number PID2019-105552RB-C43 and support from the Agencia Canaria de Investigación, Innovación y Sociedad de la Información (ACIISI) under the European FEDER (FONDO EUROPEO DE DESARROLLO REGIONAL) de Canarias 2014-2020 grant No. PROID2021010078. This paper made use of the IAC Supercomputing facility HTCONDOR (http://research.cs.wisc.edu/htcondor/), partly financed by the Ministry of Economy and Competitiveness with FEDER funds, code IACA13-3E-2493. We acknowledge the use of the Legacy Archive for Microwave Background Data Analysis (LAMBDA), part of the High Energy Astrophysics Science Archive Center (HEASARC). HEASARC/LAMBDA is a service of the Astrophysics Science Division at the NASA Goddard Space Flight Center. We acknowledge the use of data provided by the Centre d'Analyse de Données Etendues (CADE), a service of IRAP-UPS/CNRS [http://cade.irap.omp.eu, Paradis et al. (2012)]. This research has made use of the SIMBAD data base, operated at CDS, Strasbourg, France (Wenger et al. 2000). This work has made use of S-band Polarisation All Sky Survey (S-PASS) data. Based on observations obtained with Planck (http://www.esa.int/Planck), an ESA science mission with instruments and contributions directly funded by ESA Member States, NASA, and Canada. Some of the presented results are based on observations obtained with the QUIJOTE experiment (http://research.iac.es/proyecto/quijote). Some of the results in this paper have been derived using the healpy and HEALPIX packages (Górski et al. 2005; Zonca et al. 2019). We have also used SCIPY (Virtanen et al. 2020), EMCEE (Foreman-Mackey et al. 2013), NUMPY (Harris et al. 2020), MATPLOTLIB (Hunter 2007), CORNER (Foreman-Mackey 2016), and ASTROPY (Astropy Collaboration 2013, 2018) PYTHON packages.

DATA AVAILABILITY

The set of 10 parameter maps described in Section 3 for the default case (with QUIJOTE-MFI data considered) can be downloaded from the QUIJOTE web page,[18] as well as from the RADIOFOREGROUNDS[19] platform. An Explanatory Supplement describing the data format is also available. Any other derived data products described in this paper are available upon request to the QUIJOTE collaboration.

REFERENCES

Ali-Haïmoud Y., 2013, Adv. Astron., 2013, 462697
Ali-Haïmoud Y., Hirata C. M., Dickinson C., 2009, MNRAS, 395, 1055
Alves M. I. R., Davies R. D., Dickinson C., Davis R. J., Auld R. R., Calabretta M., Staveley-Smith L., 2010, MNRAS, 405, 1654
Andersen K. J. et al., 2023, A&A, 675, A13
Arce-Tord C. et al., 2020, MNRAS, 495, 3482
Astropy Collaboration, 2013, A&A, 558, A33
Astropy Collaboration, 2018, AJ, 156, 123
Battistelli E. S. et al., 2015, ApJ, 801, 111
Battistelli E. S. et al., 2019, ApJ, 877, L31
Bell A. C., Onaka T., Galliano F., Wu R., Doi Y., Kaneda H., Ishihara D., Giard M., 2019, PASJ, 71, 123
Bennett C. L. et al., 2013, ApJS, 208, 20
Berkhuijsen E. M., 1972, A&AS, 5, 263
Bianchi S. et al., 2022, A&A, 658, L8
Boggess N. W. et al., 1992, ApJ, 397, 420
Carretti E. et al., 2019, MNRAS, 489, 2330
Casassus S., Vidal M., Arce-Tord C., Dickinson C., White G. J., Burton M., Indermuehle B., Hensley B., 2021, MNRAS, 502, 589
Cepeda-Arroita R. et al., 2021, MNRAS, 503, 2927
Churchwell E. et al., 2009, PASP, 121, 213
Chuss D. T., Hensley B. S., Kogut A. J., Guerra J. A., Nofi H. C., Siah J., 2022, ApJ, 940, 59
Compiègne M. et al., 2011, A&A, 525, A103
Condon J. J., Ransom S. M., 2016, Essential Radio Astronomy, Princeton University Press, available online
Curran P. A., 2014, preprint (arXiv:1411.3816)
Davies R. D., Dickinson C., Banday A. J., Jaffe T. R., Górski K. M., Davis R. J., 2006, MNRAS, 370, 1125
de la Hoz E. et al., 2023, MNRAS, 519, 3504
de Oliveira-Costa A., Kogut A., Devlin M. J., Netterfield C. B., Page L. A., Wollack E. J., 1997, ApJ, 482, L17
de Oliveira-Costa A., Tegmark M., Gutiérrez C. M., Jones A. W., Davies R. D., Lasenby A. N., Rebolo R., Watson R. A., 1999, ApJ, 527, L9
Dickinson C. et al., 2009, ApJ, 690, 1585
Dickinson C. et al., 2010, MNRAS, 407, 2223
Dickinson C. et al., 2018, New Astron. Rev., 80, 1
Dong R., Draine B. T., 2011, ApJ, 727, 35
Draine B. T., 2011, Physics of the Interstellar and Intergalactic Medium, Princeton University Press
Draine B. T., Hensley B., 2013, ApJ, 765, 159
Draine B. T., Lazarian A., 1998a, ApJ, 494, L19
Draine B. T., Lazarian A., 1998b, ApJ, 508, 157
Draine B. T., Lazarian A., 1999, ApJ, 512, 740
Draine B. T., Li A., 2007, ApJ, 657, 810
Erickson W. C., 1957, ApJ, 126, 480
Eriksen H. K., Jewell J. B., Dickinson C., Banday A. J., Górski K. M., Lawrence C. R., 2008, ApJ, 676, 10
Fazio G. G. et al., 2004, ApJS, 154, 10
Finkbeiner D. P., 2003, ApJS, 146, 407
Fixsen D. J., 2009, ApJ, 707, 916
Foreman-Mackey D., 2016, J. Open Source Softw., 1, 24
Foreman-Mackey D., Hogg D. W., Lang D., Goodman J., 2013, PASP, 125, 306
Génova-Santos R., Rebolo R., Rubiño-Martín J. A., López-Caraballo C. H., Hildebrandt S. R., 2011, ApJ, 743, 67
Génova-Santos R. et al., 2015, MNRAS, 452, 4169
Génova-Santos R. et al., 2017, MNRAS, 464, 4107
Górski K. M., Hivon E., Banday A. J., Wand elt B. D., Hansen F. K., Reinecke M., Bartelmann M., 2005, ApJ, 622, 759
Haffner L. M., Reynolds R. J., Tufte S. L., Madsen G. J., Jaehnig K. P., Percival J. W., 2003, ApJS, 149, 405
Harper S. E. et al., 2022, MNRAS, 513, 5900
Harris C. R. et al., 2020, Nature, 585, 357
Haslam C. G. T., Salter C. J., Stoffel H., Wilson W. E., 1982, A&AS, 47, 1
Hauser M. G. et al., 1998, ApJ, 508, 25
Hazumi M. et al., 2020, in Society of Photo-Optical Instrumentation Engineers (SPIE) Conference Series. p. 114432F,
Hensley B. S., Draine B. T., 2017, ApJ, 836, 179
Hensley B., Murphy E., Staguhn J., 2015, MNRAS, 449, 809
Hensley B. S., Draine B. T., Meisner A. M., 2016, ApJ, 827, 45
Hensley B. S., Murray C. E., Dodici M., 2022, ApJ, 929, 23
Hildebrandt S. R., Rebolo R., Rubiño-Martín J. A., Watson R. A., Gutiérrez C. M., Hoyland R. J., Battistelli E. S., 2007, MNRAS, 382, 594
Hoang T., Lazarian A., 2016, ApJ, 821, 91
Hunter J. D., 2007, Comput. Sci. Eng., 9, 90
Irfan M., 2014, PhD thesis. The University of Manchester
Irfan M. O. et al., 2015, MNRAS, 448, 3572
Jonas J. L., Baart E. E., Nicolson G. D., 1998, MNRAS, 297, 977
Jones M. E. et al., 2018, MNRAS, 480, 3224
Kogut A., Banday A. J., Bennett C. L., Gorski K. M., Hinshaw G., Smoot G. F., Wright E. I., 1996, ApJ, 464, L5
Leitch E. M., Readhead A. C. S., Pearson T. J., Myers S. T., 1997, ApJ, 486, L23
Li A., Draine B. T., 2001, ApJ, 554, 778
Linden S. T., Murphy E. J., Dong D., Momjian E., Kennicutt R. C. J., Meier D. S., Schinnerer E., Turner J. L., 2020, ApJS, 248, 25

---

[18] http://research.iac.es/proyecto/cmb/quijote.
[19] http://www.radioforegrounds.eu/.

López-Caraballo C. H., Rubiño-Martín J. A., Rebolo R., Génova-Santos R., 2011, ApJ, 729, 25

Mathis J. S., Mezger P. G., Panagia N., 1983, A&A, 128, 212

Miville-Deschênes M.-A., Lagache G., 2005, ApJS, 157, 302

Murphy E. J. et al., 2010, ApJ, 709, L108

Murphy E. J., Linden S. T., Dong D., Hensley B. S., Momjian E., Helou G., Evans A. S., 2018, ApJ, 862, 20

Neugebauer G. et al., 1984, ApJ, 278, L1

Orlando E., Strong A., 2013, MNRAS, 436, 2127

Paradis D., Dobashi K., Shimoikura T., Kawamura A., Onishi T., Fukui Y., Bernard J. P., 2012, A&A, 543, A103

Peel M. W., Dickinson C., Davies R. D., Clements D. L., Beswick R. J., 2011, MNRAS, 416, L99

Peel M. W., Genova-Santos R., Dickinson C., Leahy J. P., López-Caraballo C., Fernández-Torreiro M., Rubiño-Martín J. A., Spencer L. D., 2022, Res. Notes Am. Astron. Soc., 6, 252

Planck Collaboration, 2011, A&A, 536, A20, Planck early results XX

Planck Collaboration, 2014a, A&A, 564, A45, Planck intermediate results XIV

Planck Collaboration, 2014b, A&A, 565, A103, Planck intermediate results XV

Planck Collaboration, 2014c, A&A, 571, A5, Planck 2013 results. V

Planck Collaboration, 2014d, A&A, 571, A11, Planck 2013 results. XI

Planck Collaboration, 2015a, A&A, 580, A13, Planck intermediate results. XXIII

Planck Collaboration, 2015b, A&A, 582, A28, Planck intermediate results XXV

Planck Collaboration, 2016a, A&A, 594, A10, Planck 2015 results X

Planck Collaboration, 2016b, A&A, 594, A25, Planck 2015 results XXV

Planck Collaboration, 2020, A&A, 641,A1, Planck 2018 results I

Planck Collaboration, 2020, A&A, 643, A42, Planck intermediate results. LVII

Platania P., Burigana C., Maino D., Caserini E., Bersanelli M., Cappellini B., Mennella A., 2003, A&A, 410, 847

Poidevin F. et al., 2019, MNRAS, 486, 462

Poidevin F. et al., 2023, MNRAS, 519, 3481

Reich W., 1982, A&AS, 48, 219

Reich P., Reich W., 1986, A&AS, 63, 205

Reich P., Reich W., 1988, A&AS, 74, 7

Reich W., Reich P., Fuerst E., 1990, A&AS, 83, 539

Reich P., Reich W., Furst E., 1997, A&AS, 126, 413

Reich P., Testori J. C., Reich W., 2001, A&A, 376, 861

Remazeilles M., Dickinson C., Banday A. J., Bigot-Sazy M. A., Ghosh T., 2015, MNRAS, 451, 4311

Rennie T. J. et al., 2022, ApJ, 933, 187

Rubiño-Martín J. A. et al., 2010, Astrophys. Space Sci. Proc., 14, 127

Rubiño-Martín J. A., López-Caraballo C. H., Génova-Santos R., Rebolo R., 2012, Adv. Astron., 2012, 351836

Rubiño-Martín J. A. et al., 2023, MNRAS, 519, 3383

Rybicki G. B., Lightman A. P., 1979, Radiative processes in astrophysics, Wiley-Interscience

Scaife A. M. M. et al., 2010, MNRAS, 406, L45

Schlegel D. J., Finkbeiner D. P., Davis M., 1998, ApJ, 500, 525

Silsbee K., Ali-Haïmoud Y., Hirata C. M., 2011, MNRAS, 411, 2750

Smoot G. et al., 1990, ApJ, 360, 685

Stevenson M. A., 2014, ApJ, 781, 113

Tibbs C. T., Scaife A. M. M., Dickinson C., Paladini R., Davies R. D., Davis R. J., Grainge K. J. B., Watson R. A., 2013, ApJ, 768, 98

Tibbs C. T., Israel F. P., Laureijs R. J., Tauber J. A., Partridge B., Peel M. W., Fauvet L., 2018, MNRAS, 477, 4968

Todorović M. et al., 2010, MNRAS, 406, 1629

Tramonte D. et al., 2023, MNRAS, 519, 3432

Vidal M., Dickinson C., Harper S. E., Casassus S., Witt A. N., 2020, MNRAS, 495, 1122

Virtanen P. et al., 2020, Nature Methods, 17, 261

Watson R. A., Rebolo R., Rubiño-Martín J. A., Hildebrandt S., Gutiérrez C. M., Fernández-Cerezo S., Hoyland R. J., Battistelli E. S., 2005, ApJ, 624, L89

Wehus I. K. et al., 2017, A&A, 597, A131

Wenger M. et al., 2000, A&AS, 143, 9

Werner M. W. et al., 2004, ApJS, 154, 1

Wheelock S. L. et al., 1994, IRAS sky survey atlas: Explanatory supplement, available here. NASA STI/Recon Technical Report N

Xie Y., Ho L. C., 2022, ApJ, 925, 218

Ysard N., Juvela M., Verstraete L., 2011, A&A, 535, A89

Ysard N., Miville-Deschênes M.-A., Verstraete L., Jones A. P., 2022, A&A, 663, A65

Zonca A., Singer L., Lenz D., Reinecke M., Rosset C., Hivon E., Gorski K., 2019, J. Open Source Softw., 4, 1298

SUPPORTING INFORMATION

Supplementary data are available at *MNRASL* online.

suppl_data

This paper has been typeset from a TEX/LATEX file prepared by the author.